PHYSICAL REVIEW D

PARTICLES AND FIELDS

THIRD SERIES, VOLUME 27, NUMBER 5 1 MARCH 1983

Inclusive production of hadrons at high P_T in 200 and 300 GeV $\pi^- p$ and π^--nucleus collisions

H. J. Frisch, N. D. Giokaris,[*] J. M. Green,[†] C. Grosso-Pilcher, M. D. Mestayer,[‡]
L. Schachinger,[§] M. J. Shochet, and M. L. Swartz
Enrico Fermi Institute and Department of Physics, The University of Chicago, Chicago, Illinois 60637

P. A. Piroué, B. G. Pope, and R. L. Sumner
Department of Physics, Joseph Henry Laboratories, Princeton University, Princeton, New Jersey 08544

(Received 9 August 1982)

Measurements of the production cross sections at large values of transverse momentum (P_T) for $\pi^\pm$, $K^\pm$, p, and $\bar{p}$ in 200 and 300 GeV $\pi^- p$ collisions are presented. The dependences of the cross section on P_T and the transverse scaling variable $x_T = 2P_T/\sqrt{s}$ are discussed. The ratios of production of different particle types, such as π^-/π^+, K^+/π^+, etc., are given, and are shown to be quite different from those in pp collisions. Data have been taken at three laboratory angles; the angular dependence is given and compared with theoretical models. Data on three nuclear targets allow an evaluation of the atomic-weight (A) dependence.

I. INTRODUCTION

In this paper we present the cross sections measured in an experiment on single-hadron production in 200 and 300 GeV π^--nucleus collisions over the P_T range $0.8 < P_T < 6.4$ GeV/c. The targets were hydrogen (H), beryllium (Be), copper (Cu), and tungsten (W). Spectra in P_T were measured at three laboratory angles by changing the angle of the incoming 200-GeV pion beam. These angles correspond, for relativistic secondaries, to pion—single-nucleon center-of-mass angles of 67°, 79°, and 90°. Data were also taken with a proton beam so that a comparison of the production by pions and protons could be made. A judicious selection of the many combinations of the two beam energies, the two

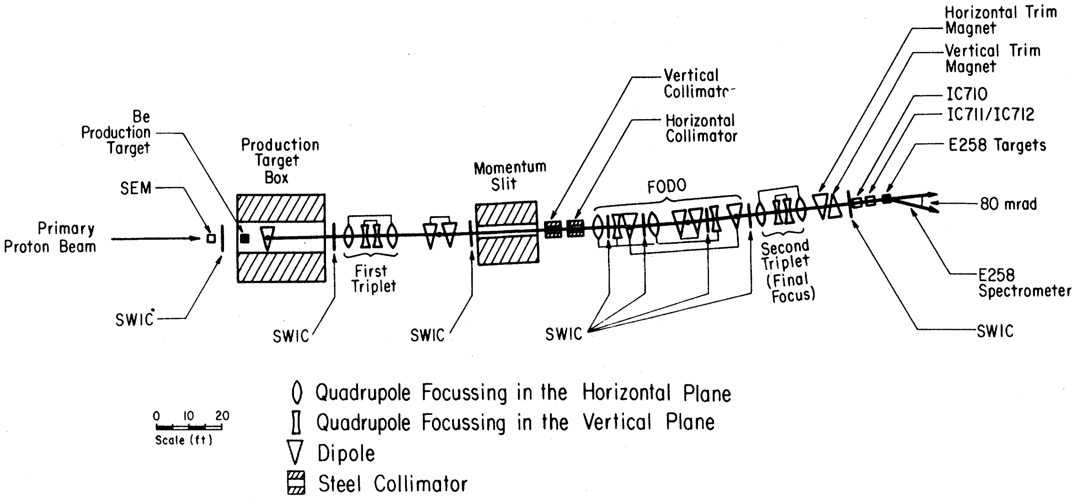

FIG. 1. A schematic view of the Proton West high-intensity secondary beam line at Fermilab (not to scale). Magnets connected with the same line were connected electrically in series.

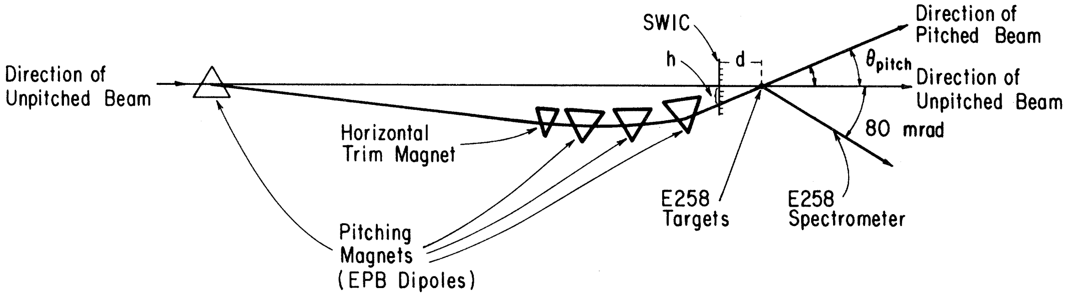

FIG. 2. The horizontal pitching magnets used to change the targeting angle.

beam particles (π^- and proton), the three laboratory angles, the two polarities of secondaries, and the four targets was explored.

The purpose of this paper is to present the numerical data, i.e., the cross sections for the separate particle types $\pi^\pm$, $K^\pm$, p, and $\bar{p}$ which are produced. We have published previously several of the results of the experiment in short papers.[1,2] More detail and the full numerical values are presented here. Full details can be found in Refs. 3 and 4.

This experiment differs in capability from preceding experiments on high-P_T particle production in $\pi^- p$ collisions in several ways. The pioneering experiment of Donaldson *et al.*[5] measured the production of neutral particles (π^0, η^0,...) rather than charged particles, and consequently has no data on the relative production of $\pi^\pm$,$K^\pm$, p, and $\bar{p}$. Although the experiment by Donaldson *et al.* was less sensitive than the one we report, their conclusions on the cross sections and the relative production of pions by π^- versus protons are well substantiated by our data.

The jet experiment of Bromberg *et al.*[6] has also measured single-charged-particle production. Direct comparisons are somewhat difficult as their single-particle sensitivity is approximately three orders of magnitude less than ours, and their particle identification is significantly poorer.

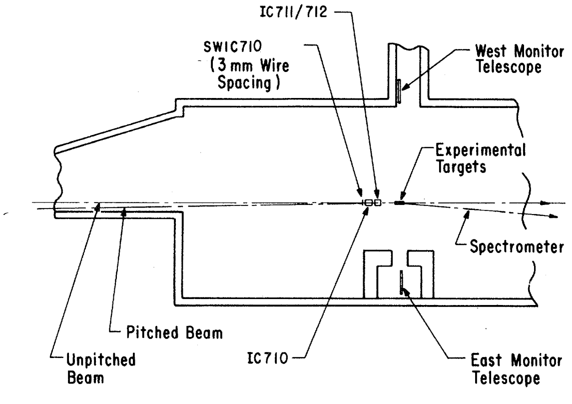

FIG. 3. The target and beam monitors.

Corcoran *et al.*[7] have measured single-π^0 production as well as jets. Their data on single π^0's are comparable to the results of Donaldson *et al.*

This paper is organized as follows. Section II describes both the high-intensity pion beam and the spectrometer. The small-aperture magnetic spectrometer is quite similar to the one used in the past by our Chicago-Princeton collaboration[8] to make measurements of single-particle production at high P_T by incoming protons. Section II thus puts particular emphasis on the differences in technique between this experiment and the previous ones; these changes were largely forced by the differences between the finely focused high-intensity proton beam and the much larger and less intense pion beam.

Section III discusses the analysis of the data. Both the necessary corrections and the estimates of assigned errors are discussed.

The results for the data taken with the hydrogen target are presented in Sec. IV. The cross sections themselves, the ratios of the different particle types produced, and the ratios of the relative production of particles by incoming pions to that by protons are tabulated. It is these tables, and the analogous ones in Sec. V for the nuclear targets, which are the heart of the paper. Section V discusses the dependence of the cross sections on the atomic weight of the target: an "anomalous" atomic-weight dependence is observed in pion-nucleus collisions much as is seen in proton-nucleus collisions.[8]

The conclusions are summarized in Sec. VI.

II. DESCRIPTION OF THE APPARATUS AND THE PION BEAM

This experiment (Fermilab E258) was the first to use the high-intensity pion beam in the Proton West area at Fermilab.[9] We proposed[10] it following a series of experiments investigating high transverse momentum interactions with proton beams.[8]

The spectrometer differed from the one used previously in its larger-aperture magnets, its shorter length (and hence greater momentum bite), and in

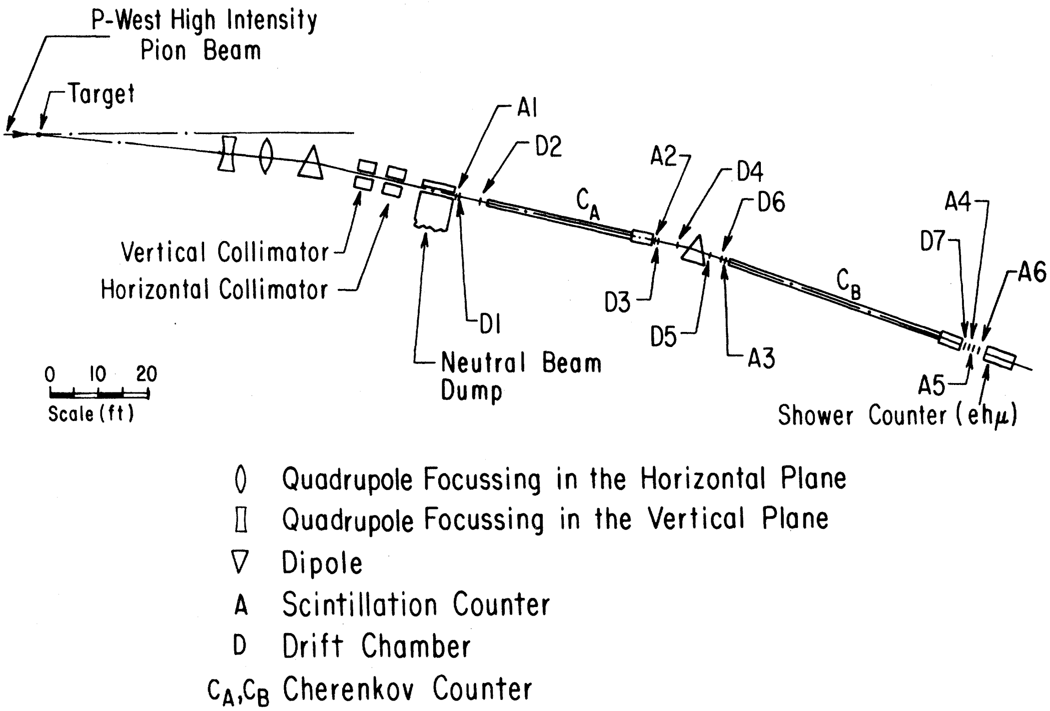

FIG. 4. Plan view of the spectrometer.

the replacement of counter hodoscopes by drift chambers. The larger spot and difficult intensity range (10^9—10^{10} π/sec) of the pion beam also led to some changes in the monitors, particularly in the addition of the etched-foil ion chambers described below.

A. Proton West high-intensity beam

Primary protons were transported by the Proton West beam line to the 1-absorption-length Be production target (see Fig. 1). The intensity of the primary proton beam was measured by a secondary-emission monitor (SEM) a few feet upstream of the production target. A typical proton beam intensity during the experiment was 3×10^{12} protons/pulse.

The high-intensity pion beam line viewed the production target at an angle of 0°. Figure 1 shows the elements of the beam. The dipole magnet immediately after the production target selected the sign of the secondary beam and swept out of the beam channel all particles whose momenta differed from the beam momentum by more than 40%. The first quadrupole triplet took the flux emerging from the target box and, with the dipoles immediately downstream, formed a horizontally dispersed vertical focus at the position of the momentum slit.

The dispersion at the momentum slit was 3 mm/%; the maximum momentum bite of the beam was 5% (σ). The momentum slit was followed by

TABLE I. The physical properties of the targets.

			Length		
Target	Atomic weight	Density (g/cm^3)	(Inches) ±0.001	(Number of absorption lengths for 200 GeV π^-'s)	(Number of absorption lengths for 200 GeV protons)
H[a]	1.01	0.071	20.000	0.043	0.069
Be (long)	9.01	1.85	7.220	0.34	0.49
Be (short)	9.01	1.85	1.000	0.047	0.068
Cu	63.54	8.96	2.910	0.41	0.51
W[b]	183.85	19.3	2.031	0.46	0.56

[a] The hydrogen was at 20.4 K (boiling point) and atmospheric pressure.

[b] Kennametal W-2. The measured density of the W target was 18.22 g/cm^3 because it contained a small fraction of Ni, Cu, and Fe as a binder. The W-target cross sections were corrected for these impurities. (The correction was 3.5% ±1%).

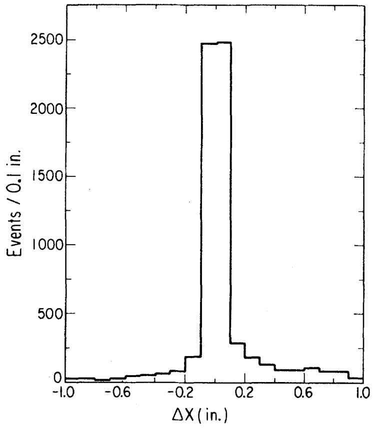

FIG. 5. Distribution of the difference Δx of the x positions between all possible combinations of upstream and downstream x tracks at the middle of the downstream dipole for a 20 GeV/c run.

three bending magnets, and a system of four singlet quadrupoles with alternating polarities forming a focusing-defocusing (FODO) channel. The three bending magnets corrected the dispersion and the angle-momentum correlation. The FODO channel transmitted the beam to the final focusing triplet. Chromatic aberration is unfortunately not corrected in this beam.

The FODO system was followed by a targeting triplet which focused the beam at the position of the experimental target. The horizontal and vertical trim dipoles, immediately after the final triplet, were used for positioning the beam at the target.

Figure 2 shows the system of four additional dipole magnets immediately upstream of the experimental target used to change the targeting angle of the incident beam by ±16 mrad.

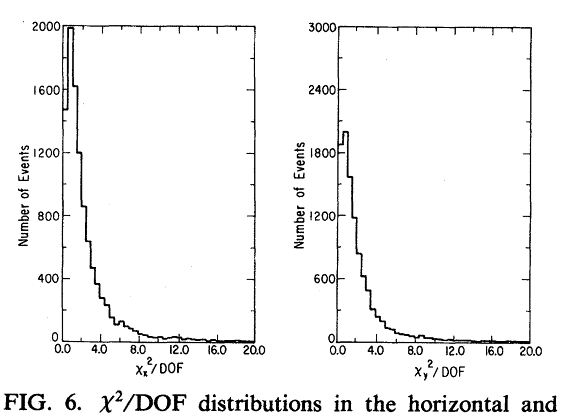

FIG. 6. χ^2/DOF distributions in the horizontal and vertical planes for tracks with the best fit for a 25 GeV/c run.

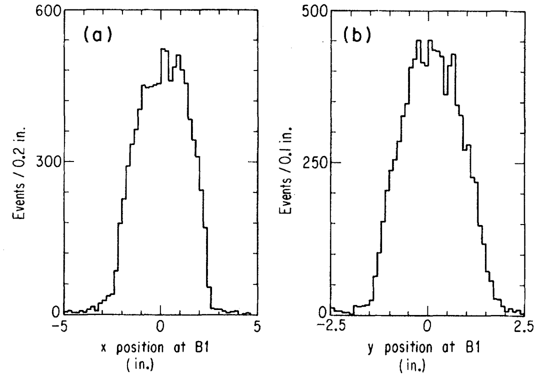

FIG. 7. (a) Distribution of the horizontal position extrapolated to the upstream magnet $B1$ for a 25 GeV/c run. (b) The same for the vertical position.

The theoretical acceptance of the beam, as found from the CERN HALO Monte Carlo program,[11] was $\Delta\Omega\,\Delta p/p = 110$ μsr %. The spot size at our target was approximately 1 in. (horizontal)×0.7 in. (vertical) (full width at half maximum).

Primary protons could also be transported down the beam line to the experimental target by removing the production target. Data with 200 GeV primary protons were taken to normalize the data taken in this experiment to previous data taken with a proton beam and a similar spectrometer in the Proton East area.[8]

B. Beam Monitors

The area surrounding the experimental target is shown in more detail in Fig. 3. Sixty inches upstream of the experimental target a segmented-wire ion chamber (SWIC) was located to check the position and the shape of the secondary beam. Two ion chambers IC710 and IC711/IC712 measured the beam flux.

Each ion chamber was contained in a cylindrical

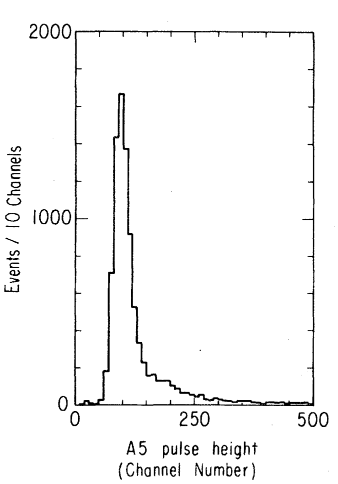

FIG. 8. Distribution of pulse height in the last trigger counter, $A4$, for a 25 GeV/c run.

TABLE II. The values of the eight cuts on the trajectories. Also shown are the percentages of the triggers eliminated by each cut for a spectrometer momentum setting of 25 GeV/c.

Cut	Limits	Fraction eliminated
χ^2	≤ 11	6%
$D7$-chamber aperture	± 6 in. (horiz) $\times \pm 3$ in. (vert.)	2%
Downstream dipole aperture ($B2$)	± 2.68 in. (horiz.) $\times \pm 1.48$ in. (vert.)	0.6%
Upstream dipole aperture ($B1$)	± 2.68 in. (horiz.) $\times \pm 1.48$ in. (vert.)	2%
Downstream quadrupole aperture ($Q2$)	± 2.52 in. (horiz.) $\times \pm 1.6$ in. (vert.)[a]	4%
Upstream quadrupole aperture ($Q1$)	± 1.6 in. (horiz.) $\times \pm 3.0$ in. (vert.)[a]	0.1%
$A4$ pulse height	≥ 50 channels	0.4%
$\Delta p/p_0$	$-0.15 \leq \Delta p/p_0 \leq 0.20)$	0.2%
Hydrogen target projections	-3.2 in. $< x < 2.4$ in.	0.1%
or	$\lvert y \rvert < 0.8$ in.	
Nuclear target projections	$\lvert x \rvert < 1.6$ in.	1.5%
	$\lvert y \rvert < 0.7$ in.	

[a] The quadrupole cuts were elliptical. The numbers given are the horizontal and vertical semiaxes of the ellipses.

aluminum tube 6 in. in diameter. The electrodes of IC711/IC712, however, were divided into two parts by etching the foils: the inside part (IC712) had a cross section equal to the cross section of the nuclear targets (1.25 in.×0.75 in.), and the outside part (IC711) was the complement of the inside. In this way the fraction of the beam that hit the nuclear targets could be measured by IC712.

At an angle of 90° in the laboratory frame and a distance from the target of 15 and 20 ft, respectively, were the East and the West 90° monitors (see Fig. 3), each consisting of a three-counter telescope. The 90° monitors were used, together with the ion chambers, to measure the amount of beam interacting in the target.

C. Secondary yields

The beam line was run at 200 and 300 GeV for negative particles. The yields per 400 GeV proton are 4.7×10^{-4} and 5.1×10^{-5} for 200 and 300 GeV secondary particles. For 350 GeV protons, the 200 GeV yield drops to 2.9×10^{-4}.

The beam particle composition was not measured. Measurements at small angles[12] predict that the beam was 95% π^-, 5% K^-, and less than 1% $\bar{p}$ at $x=0.5$ (200 GeV secondaries and 400 GeV incident protons), and 98% π^-, 2% K^-, and less than 0.2% $\bar{p}$ at $x=0.75$ (300 GeV secondaries and 400 GeV incident protons).

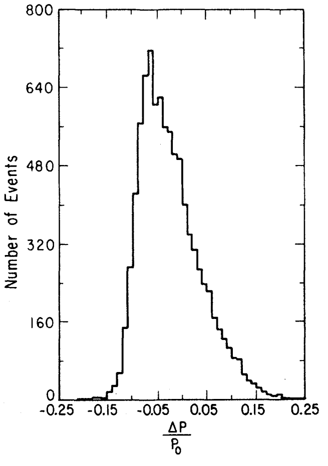

FIG. 9. $\Delta P/P_0$ distribution for a 25 GeV/c run. All other cuts but the $\Delta P/P_0$ and target cuts were applied to the data.

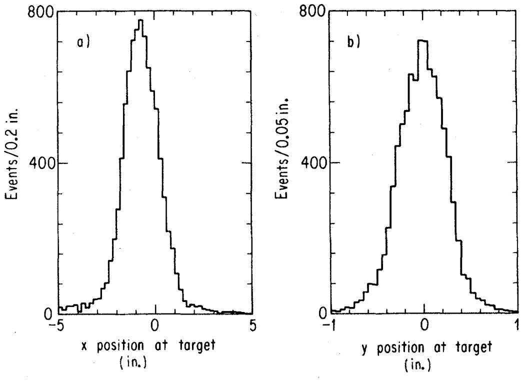

FIG. 10. (a) Distribution of the vertical position of the target for a 25 GeV/c run. (b) Distribution of the horizontal position of the target for a 25 GeV/c run.

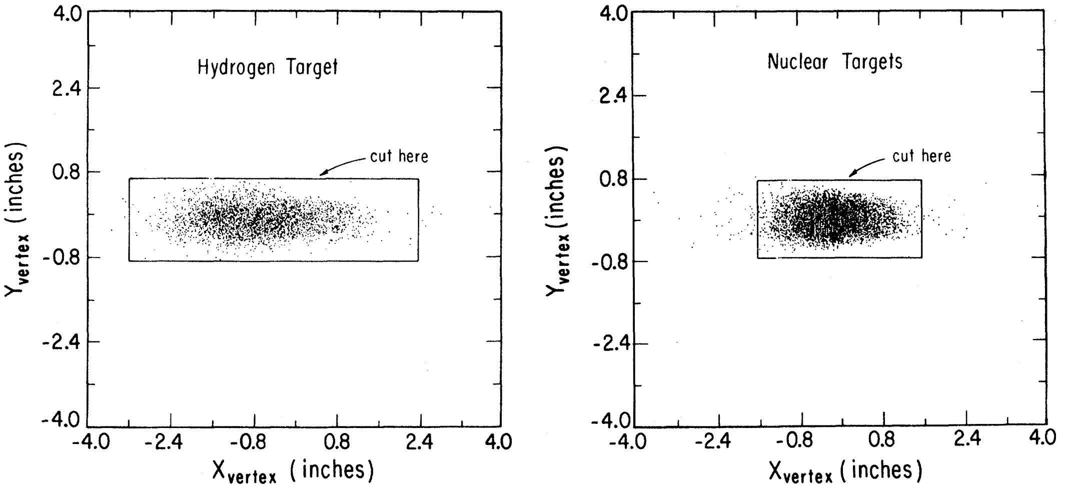

FIG. 11. The projected horizontal versus vertical positions of tracks at the experimental target for 25 GeV/c runs with the hydrogen and tungsten targets. All but the target cuts have been applied to the data.

D. The magnetic spectrometer

The spectrometer is shown in Fig. 4. The first optical element was a quadrupole doublet (Fermilab 4Q120)[13] which focused particles originating at the target onto the last trigger counter ($A4$) of the spectrometer. The horizontal and vertical magnifications of this doublet were 3 and 6, respectively, at the end of the spectrometer. The doublet was followed by a dipole (Fermilab 6-3-120)[13] set to a 16-mrad angular bend, which selected the sign and the momentum of the particles accepted by the spectrometer. Downstream of this dipole a set of two collimators and the heavily shielded neutral beam dump were used to stop all particles with momenta far from the central momentum of the spectrometer.

The part of the spectrometer downstream of this shielding consisted of scintillator trigger counters ($A1, A2, \ldots, A4$), a second dipole (also with a 16-mrad bend (with drift chambers ($D1, D2, \ldots, D7$) on either side to measure the momentum of individual particles with high precision, and two Cherenkov counters (C_A, C_B) for $\pi/K/p$ identification. At the end of the spectrometer sat a shower counter ($eh\mu$) to separate muons from hadrons.

The dispersion of the two dipoles at the position of $D7$ was 0.6 in./%, and the spectrometer integrated acceptance $\Delta\Omega\,\Delta P/P$ was 410 μsr%, with a momentum bite of approximately 20%.

A liquid-hydrogen target and three nuclear targets, beryllium (Be), copper (Cu), and tungsten (W) were used. The nuclear targets were rectangular, 1.25 in. horizontally by 0.75 in. vertically. Two Be targets of different lengths were used to check the correction to the cross sections due to absorption in the targets. The hydrogen target consisted of a 20-in.-long, 3-in.-diameter stainless-steel flask, with side walls 0.003 in. thick, and with 0.001-in.-thick hemispherical stainless-steel end windows. In Table I, a list of the targets, their lengths, and their relevant physical constants is given.

Particles were identified by the two Cherenkov counters C_A and C_B. The length of C_A was 46 ft, and of C_B was 66 ft. Each consisted of a 1-ft-

TABLE III. The ratio of identified muons to identified pions as a function of momentum.

Momentum (GeV/c)	μ/π (%)
10	7.8
15	5.7
20	4.5
25	3.7
30	3.2
40	2.4
50	1.6
60	1.2
70	0.8
80	0.5
90	0.2

TABLE IV. The invariant cross sections $E\,d^3\sigma/d^3p$ for the production of $\pi^{\pm}$, $K^{\pm}$, p, and $\bar{p}$ at a laboratory angle of 96.3 mrad (c.m. angle near 90°) in 200 GeV $\pi^- p$ collisions. The units are cm^{2}GeV^{-2}.

P_T (GeV/c)	π^+	π^-	K^+	K^-	p	$\bar{p}$
0.96	$2.18 \pm 0.18 \times 10^{-28}$	$2.54 \pm 0.21 \times 10^{-28}$	$6.51 \pm 0.59 \times 10^{-29}$	$4.91 \pm 0.46 \times 10^{-29}$	$6.35 \pm 0.53 \times 10^{-29}$	$2.49 \pm 0.22 \times 10^{-29}$
1.44	$1.87 \pm 0.15 \times 10^{-29}$	$2.26 \pm 0.18 \times 10^{-29}$	$6.07 \pm 0.51 \times 10^{-30}$	$4.76 \pm 0.41 \times 10^{-30}$	$6.63 \pm 0.55 \times 10^{-30}$	$2.75 \pm 0.23 \times 10^{-30}$
1.93	$2.17 \pm 0.18 \times 10^{-30}$	$2.43 \pm 0.20 \times 10^{-30}$	$7.43 \pm 0.71 \times 10^{-31}$	$5.62 \pm 0.58 \times 10^{-31}$	$8.40 \pm 0.74 \times 10^{-31}$	$3.54 \pm 0.36 \times 10^{-31}$
2.41	$2.50 \pm 0.12 \times 10^{-31}$	$2.97 \pm 0.14 \times 10^{-31}$	$1.03 \pm 0.05 \times 10^{-31}$	$7.72 \pm 0.41 \times 10^{-32}$	$9.12 \pm 0.46 \times 10^{-32}$	$2.81 \pm 0.16 \times 10^{-32}$
2.89	$4.07 \pm 0.21 \times 10^{-32}$	$4.73 \pm 0.25 \times 10^{-32}$	$1.68 \pm 0.11 \times 10^{-32}$	$1.14 \pm 0.09 \times 10^{-32}$	$1.27 \pm 0.08 \times 10^{-32}$	$4.13 \pm 0.39 \times 10^{-33}$
3.85	$1.38 \pm 0.11 \times 10^{-33}$	$1.33 \pm 0.11 \times 10^{-33}$	$5.55 \pm 0.71 \times 10^{-34}$	$3.70 \pm 0.57 \times 10^{-34}$	$3.02 \pm 0.44 \times 10^{-34}$	$7.18 \pm 2.14 \times 10^{-35}$
4.82	$4.85 \pm 0.99 \times 10^{-35}$	$6.05 \pm 1.10 \times 10^{-35}$	$2.46 \pm 0.73 \times 10^{-35}$	$1.58 \pm 0.61 \times 10^{-35}$	$7.98 \pm 4.03 \times 10^{-36}$	----------
5.78	$2.96 \pm 1.15 \times 10^{-36}$	$1.66 \pm 0.84 \times 10^{-36}$	$7.92 \pm 5.68 \times 10^{-37}$	$4.97 \pm 4.97 \times 10^{-37}$	$1.35 \pm 0.98 \times 10^{-36}$	----------

diameter stainless-steel tube with nonreflecting walls. The tube was bolted to a 6-ft-long optics section. Each counter had two channels. The inner channel accepted light emitted at angles from 0 to 9 mrad and the outer one was sensitive to light emitted at angles of 9 to 40 mrad. The light was focused onto a 2 in. photomultiplier (selected RCS 31 000M) in each channel. With a threshold requirement of two photoelectrons, the counters were 99% efficient when the Cherenkov angle exceeded 3.5 mrad. Both CO_2 and He gas were used as gas fillings at pressures ranging from 0.5 to 5 atm. The gas pressure was measured with a precision transducer to 0.9%. The temperature was measured at several locations along the counter with a precision of 0.5 °C. The counter walls were in thermal contact with a water jacket in which the water was continuously circulated so that the temperature of the gas was uniform to within the measurement accuracy over the length of the counter.

In order to distinguish muons from hadrons a lead/lucite calorimeter (indicated as $eh\mu$ in Fig. 4) was used at the end of the spectrometer. It consisted of seven modules. The first module consisted of 18 layers of $\frac{1}{4}$-in. lead alternating with 18 layers of $\frac{1}{2}$-in. lucite. This depth corresponds to 30 radiation lengths and 1.4 absorption lengths. Each of the remaining six modules consisted of 20 layers of $\frac{1}{4}$-in. lead alternating with 20 layers of $\frac{1}{8}$-in. lucite. Cherenkov light was focused by the curved ends of the lucite and guided by aluminized mylar light cones onto 58DVP photomultiplier tubes. The first module had six photomultipliers (each sampling three lead-lucite layers) and each of the remaining six modules was viewed by one photomultiplier.

E. Drift chambers

The seven drift chambers $D1, \ldots, D7$ (see Fig. 4) in the spectrometer were used to find the trajectory of each particle, determine its momentum in conjunction with the second dipole magnet, and extrapolate the track through the upstream part of the spectrometer back to the target. Each of the chambers consisted of either one or two modules, each module containing two sense planes offset by half a cell. One of the two sense planes in each module had seven and the other eight wires, except in $D7$ where the one plane had 12 and the other 13 wires. The sense planes were $\frac{1}{2}$ in. apart, and the drift space was $\frac{1}{2}$ in. Each of the seven chambers had a module with vertical wires (x wires). Chambers $D1$–$D3$, $D6$, and $D7$ also had a module with wires rotated by 10° from the vertical (u wires).

The high-voltage wires were set to a negative potential of 3.8 kV; the sense wires were at virtual ground. An equal (by volume) mixture of argon and ethane (C_2H_6) was used for the drift-chamber gas. A detailed discussion of the multihit drift-chamber electronics is given in Ref. 14.

Typical drift-chamber plane efficiencies were 98%, varying from plane to plane from a minimum value of 95% to a maximum of 99%. The chamber resolution of 260 μ allowed a momentum resolution of 1% for momenta larger than 30 GeV/c.

F. Data acquisition

The trigger consisted of a four-fold coincidence $A1 \cdot A2 \cdot A3 \cdot A4$. (See Fig. 4). Because of the large range in the cross section measured by this experiment (10 orders of magnitude) a dual data acquisition system was employed. One system read out all the information for each event. Typically 60 to 100 events per spill could be read out and recorded on tape by the PDP-9 computer. At low transverse momentum, the high event rate led to a large computer deadtime. A second, deadtimeless, system which involved only the scintillator trigger logic and scalars was read out at the end of each machine pulse.

Other data, such as the magnet currents, and the Cherenkov pressures and temperatures were continuously monitored and recorded by the computer. Various on-line display programs supplied a continuous monitoring of the operation of the apparatus.

III. DATA ANALYSIS

The goal of the data analysis was to determine the invariant cross section as a function of the transverse momentum P_T for the inclusive production of each one of the long-lived hadrons $\pi^{\pm}$, $K^{\pm}$, p, and $\bar{p}$ in π^- nucleus collisions. Because the cross sections are steep in P_T, falling about one order of magnitude for every 1 GeV/c in P_T, accurate determinations of the momentum scale and of the spectrometer acceptance are necessary. The overall normalization, although less crucial, is also not easily determined as the incoming beam is too intense to count in a straightforward manner.

The invariant cross section for the production of particle type i ($i=\pi,K,p$) by a beam of type b (π^- or p) is given by

$$E\frac{d^2\sigma_i}{dp^3}=\left[\frac{N_i}{N_b}\right]\left[\frac{A}{\rho L N_A}\right]\left[\frac{E}{p^3}\right]\times\left[\frac{1}{\Delta\Omega\,\Delta p/p}\right]\left[\frac{1}{C_{\rm abs}}\right],$$

TABLE V. The invariant cross section $E\,d^3\sigma/d^3p$ for the production of $\pi^{\pm}$, $K^{\pm}$, p, and $\bar{p}$ at a laboratory angle of 80 mrad (c.m. angle near 90°) in 300 GeV $\pi^- p$ collisions. The units are cm^2 GeV^{-2}.

P_T (GeV/c)	π^+	π^-	K^+	K^-	p	$\bar{p}$
0.80	$5.75 \pm 0.43 \times 10^{-28}$	$6.37 \pm 0.48 \times 10^{-28}$	$1.36 \pm 0.13 \times 10^{-28}$	$1.19 \pm 0.12 \times 10^{-28}$	$1.22 \pm 0.11 \times 10^{-28}$	$5.49 \pm 0.50 \times 10^{-29}$
1.20	$6.83 \pm 0.51 \times 10^{-29}$	$8.24 \pm 0.61 \times 10^{-29}$	$2.00 \pm 0.16 \times 10^{-29}$	$1.48 \pm 0.12 \times 10^{-29}$	$2.26 \pm 0.18 \times 10^{-29}$	$1.02 \pm 0.08 \times 10^{-29}$
1.60	$1.05 \pm 0.09 \times 10^{-29}$	$1.21 \pm 0.10 \times 10^{-29}$	$3.68 \pm 0.32 \times 10^{-30}$	$2.92 \pm 0.26 \times 10^{-30}$	$3.80 \pm 0.34 \times 10^{-30}$	$1.65 \pm 0.16 \times 10^{-30}$
2.00	$1.86 \pm 0.10 \times 10^{-30}$	$2.07 \pm 0.10 \times 10^{-30}$	$7.72 \pm 0.51 \times 10^{-31}$	$4.74 \pm 0.34 \times 10^{-31}$	$7.08 \pm 0.51 \times 10^{-31}$	$3.65 \pm 0.28 \times 10^{-31}$
2.40	$3.96 \pm 0.25 \times 10^{-31}$	$4.54 \pm 0.28 \times 10^{-31}$	$1.59 \pm 0.12 \times 10^{-31}$	$1.27 \pm 0.09 \times 10^{-31}$	$1.20 \pm 0.10 \times 10^{-31}$	$5.35 \pm 0.46 \times 10^{-32}$
3.20	$2.35 \pm 0.21 \times 10^{-32}$	$2.85 \pm 0.21 \times 10^{-32}$	$1.03 \pm 0.13 \times 10^{-32}$	$7.96 \pm 0.88 \times 10^{-33}$	$6.14 \pm 0.86 \times 10^{-33}$	$1.85 \pm 0.34 \times 10^{-33}$
4.00	$1.84 \pm 0.25 \times 10^{-33}$	$2.32 \pm 0.27 \times 10^{-33}$	$1.12 \pm 0.20 \times 10^{-33}$	$5.50 \pm 1.10 \times 10^{-34}$	$2.67 \pm 0.87 \times 10^{-34}$	$1.64 \pm 0.64 \times 10^{-34}$
4.80	$1.02 \pm 0.29 \times 10^{-34}$	$2.49 \pm 0.47 \times 10^{-34}$	$8.80 \pm 2.80 \times 10^{-35}$	$1.80 \pm 1.10 \times 10^{-35}$	$3.50 \pm 1.90 \times 10^{-35}$	----------------
5.60	----------------	$3.80 \pm 1.30 \times 10^{-35}$	----------------	----------------	----------------	----------------

TABLE VI. Results of the fits of the 200 and 300 GeV cross sections to the form $E\,d^3\sigma/d^3p \simeq (1/P_T{}^n)\,(1-x_T)^b$. Also given for comparison are the values of pp collisions from Ref. 8.

	π^-p			pp	
	n	b	χ^2/DOF	n	b
π^+	8.6±0.5	7.0±0.6	6.6/4	8.2±0.5	9.0±0.5
π^-	7.5±0.5	8.9±0.7	2.2/5	8.5±0.5	9.9±0.5
K^+	7.3±0.6	8.6±1.1	1.1/4	8.4±0.7	8.3±0.6
K^-	8.4±0.5	8.2±0.5	9.3/4	10.1±1.5	11.5±1.3
p	9.9±0.8	6.4±1.5	1.8/4	11.8±1.6	7.3±1.1
$\bar{p}$	9.8±1.2	8.1±0.8	0.96/1	8.8±1.8	14.2±2.0

where

N_i is the number of particles of type i observed,

N_b is the number of beam particles incident on the target,

A, ρ, and L are the atomic weight, density, and length of the target (see Table I for the values),

N_A is Avogadro's number,

E and p are the energy and momentum of the detected hadron,

$\Delta\Omega\,\Delta p/p$ is the acceptance of the spectrometer

TABLE VII. The ratios of the invariant cross sections of particles produced in 200 and 300 GeV π^-p collisions. Similar ratios measured by this experiment in 200 GeV pp collisions are also included.

			$\overline{\bar{p}/p\ K^+/\pi^+\ K^-/\pi^-}$ 200 GeV π^- beam				
P_T (GeV/c)	π^-/π^+	K^-/K^+	$\bar{p}/p$	K^+/π^+	K^-/π^-	p/π^+	$\bar{p}/\pi^-$
0.96	1.17 ± 0.02	0.75 ± 0.05	0.39 ± 0.02	0.30 ± 0.01	0.19 ± 0.01	0.29 ± 0.01	0.098 ± 0.004
1.44	1.21 ± 0.02	0.78 ± 0.03	0.41 ± 0.01	0.32 ± 0.01	0.21 ± 0.01	0.35 ± 0.01	0.122 ± 0.008
1.93	1.12 ± 0.04	0.76 ± 0.06	0.42 ± 0.03	0.34 ± 0.02	0.23 ± 0.02	0.30 ± 0.02	0.15 ± 0.01
2.41	1.19 ± 0.02	0.75 ± 0.03	0.31 ± 0.01	0.41 ± 0.01	0.26 ± 0.01	0.36 ± 0.01	0.094 ± 0.004
2.89	1.16 ± 0.04	0.68 ± 0.06	0.33 ± 0.03	0.41 ± 0.02	0.24 ± 0.02	0.31 ± 0.02	0.087 ± 0.008
3.85	0.96 ± 0.09	0.67 ± 0.13	0.24 ± 0.08	0.40 ± 0.06	0.28 ± 0.05	0.22 ± 0.03	0.05 ± 0.02
4.82	1.25 ± 0.33	0.64 ± 0.31	-----------	0.51 ± 0.18	0.26 ± 0.10	0.16 ± 0.09	------------
5.78	0.56 ± 0.36	0.63 ± 0.63	-----------	0.27 ± 0.22	0.30 ± 0.30	0.46 ± 0.37	------------
			300 GeV π^- beam				
0.80	1.11 ± 0.03	0.88 ± 0.08	0.45 ± 0.03	0.24 ± 0.02	0.19 ± 0.01	0.21 ± 0.01	0.086 ± 0.005
1.20	1.21 ± 0.03	0.74 ± 0.05	0.45 ± 0.02	0.29 ± 0.01	0.18 ± 0.01	0.33 ± 0.02	0.124 ± 0.005
1.60	1.15 ± 0.04	0.79 ± 0.06	0.43 ± 0.04	0.35 ± 0.02	0.24 ± 0.01	0.36 ± 0.02	0.14 ± 0.01
2.00	1.11 ± 0.04	0.62 ± 0.05	0.52 ± 0.04	0.42 ± 0.03	0.24 ± 0.02	0.38 ± 0.03	0.18 ± 0.01
2.40	1.15 ± 0.08	0.80 ± 0.07	0.45 ± 0.05	0.40 ± 0.03	0.28 ± 0.02	0.30 ± 0.03	0.12 ± 0.01
3.20	1.21 ± 0.12	0.77 ± 0.12	0.30 ± 0.07	0.44 ± 0.06	0.28 ± 0.03	0.26 ± 0.04	0.06 ± 0.01
4.00	1.26 ± 0.21	0.49 ± 0.13	0.61 ± 0.22	0.61 ± 0.13	0.24 ± 0.05	0.15 ± 0.05	0.07 ± 0.03
4.80	2.44 ± 0.80	0.20 ± 0.15	-----------	0.86 ± 0.37	0.07 ± 0.05	0.34 ± 0.21	-----------
			200 GeV p beam				
0.96	0.86 ± 0.02	0.56 ± 0.05	0.206 ± 0.014	0.24 ± 0.01	0.16 ± 0.01	0.31 ± 0.02	0.075 ± 0.005
1.44	0.83 ± 0.02	0.50 ± 0.03	0.146 ± 0.007	0.32 ± 0.01	0.20 ± 0.01	0.53 ± 0.01	0.094 ± 0.002
1.93	0.77 ± 0.01	0.46 ± 0.02	0.120 ± 0.005	0.36 ± 0.01	0.21 ± 0.01	0.60 ± 0.02	0.093 ± 0.002
2.41	0.83 ± 0.01	0.47 ± 0.01	0.091 ± 0.004	0.40 ± 0.01	0.22 ± 0.01	0.61 ± 0.01	0.067 ± 0.002
2.88	0.70 ± 0.03	0.37 ± 0.03	0.067 ± 0.006	0.41 ± 0.03	0.22 ± 0.01	0.59 ± 0.04	0.057 ± 0.004
3.85	0.58 ± 0.04	0.26 ± 0.04	0.033 ± 0.008	0.43 ± 0.04	0.19 ± 0.03	0.49 ± 0.04	0.028 ± 0.006
4.82	0.37 ± 0.10	0.25 ± 0.25	-------------	0.52 ± 0.17	0.04 ± 0.04	0.34 ± 0.13	0.028 ± 0.006

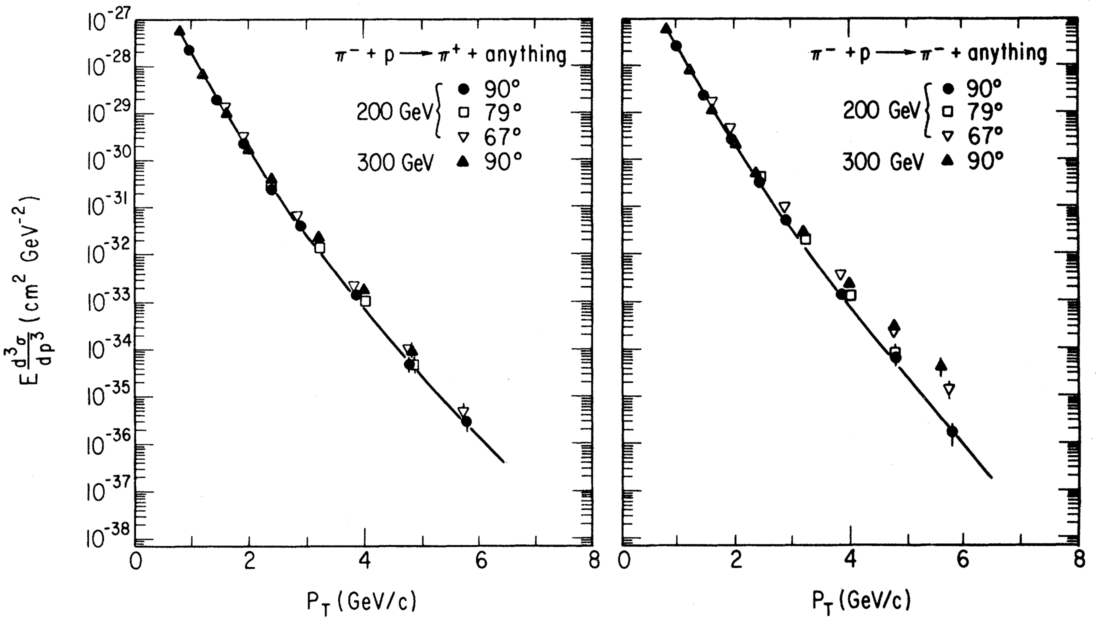

FIG. 12. Cross sections for $\pi^{\pm}$ production in 200 GeV and 300 GeV $\pi^- p$ collisions versus P_T. The angles given are the corresponding angles in the c.m. for highly relativistic particles.

TABLE VIII. The center-of-mass angles which correspond to the spectrometer laboratory angles at which data were taken.

Particle produced	π			K			p		
Beam-spectrometer angle in the laboratory	96.3 mrad	80 mrad	63.7 mrad	96.3 mrad	80 mrad	63.7 mrad	96.3 mrad	80 mrad	63.7 mrad
Momentum (GeV/*c*)									
10	90.4°	----	----	97.2°	----	----	115.0°	----	----
15	90.0°	----	----	93.1°	----	----	101.6°	----	----
20	89.9°	----	----	91.7°	----	----	96.5°	----	----
25	89.9°	----	66.9°	91.0°	----	68.3°	94.1°	----	72.5°
30	89.8°	79.3°	66.8°	90.6°	80.2°	67.8°	92.8°	82.7°	70.7°
40	89.8°	79.2°	----	90.2°	79.7°	----	91.5°	81.2°	----
45	----	----	66.8°	----	----	67.2°	----	----	68.5°
50	89.8°	79.2°	----	90.0°	79.6°	----	90.9°	80.5°	----
60	89.8°	79.2°	66.8°	90.0°	79.4°	67.0°	90.5°	80.1°	67.7°
75	----	----	66.7°	----	----	66.9°	----	----	67.4°
90	----	----	66.7°	----	----	66.8°	----	----	67.2°

(410 μsr %),

C_{abs} is a target absorption factor which depends on both the absorption length of the beam particle, λ_b, and the absorption length of the produced particle, λ_i,

$$C_{\text{abs}}=\left[\frac{\lambda_b\lambda_i}{L(|\lambda_b-\lambda_i|)}\right]\exp(-L/\lambda_i)$$
$$\times\left[1-\exp\left[\frac{L(|\lambda_b-\lambda_i|)}{\lambda_b\lambda_i}\right]\right].$$

A. Yield determination: Finding N_i

The reconstruction of tracks was quite straightforward as the apertures were small, the lever arms long, and there was a great deal of redundancy in the chamber system. The treatment here will consequently be brief—the reader interested in more details is referred to Refs. 3 and 4.

Particle trajectories in the spectrometer were required first to reconstruct as smooth tracks in the 143 ft of spectrometer over which they were measured. This required a hit in *either* of the drift chambers $D1$ or $D2$, either $D3$ or $D4$, and hits in two out of the three chambers $D5$, $D6$, and $D7$ (see Fig. 4). Straight lines both upstream and downstream of the second bend were required, and it was demanded that these two segments meet within 0.3 in. at the center of the bend (see Fig. 5). It was further required that the small-angle stereo wires of three out of the five chambers $D1$, $D2$, $D3$, $D6$, and $D7$ have hits and that these form a straight line in the vertical (nonbending) plane with a reasonable χ^2. A global fit was then performed, and if multiple solutions were present, the track with the best χ^2 was chosen. At a momentum of 25 GeV/c ($P_T=2.0$ GeV/c), a value where accidental triggers were negligible (94±2)% of all events taken by the computer reconstructed to this point. The (6±2)% inefficiency is consistent with known inefficiencies in the chambers and the reconstruction program.

At this point geometrical cuts were made on the data. The first cut required that the horizontal and vertical χ^2's, $\chi_x{}^2$ and $\chi_y{}^2$, for the track each be less than 11 per degree of freedom. (See Fig. 6). These loose cuts rejected 6% of the reconstructed events.

The trajectories were then extrapolated upstream, through the magnetic fields of the first bend $B1$ and the quadrupole $Q2$ and $Q1$, to the plane of the target. The track was required to pass through the apertures of chamber $D7$, and the magnets $B2$, $B1$, $Q2$, and $Q1$. A typical plot showing the projected positions at the center of $B1$ is given in Fig. 7. The cuts and their effect are given in Table II: the frac-

TABLE IX. The invariant cross sections $E\,d^3\sigma/dp^3$ for the production of $\pi^\pm$, $K^\pm$, p, and $\bar{p}$ at a laboratory angle of 80 mrad (corresponding to a laboratory angle of ~79° for relativistic particles) in 200 GeV π^-p collisions. The units are cm^2 GeV^{-2}.

P_T (GeV/c)	π^+	π^-	K^+	K^-	p	$\bar{p}$
2.40	$2.86 \pm 0.15 \times 10^{-31}$	$3.68 \pm 0.21 \times 10^{-31}$	$1.23 \pm 0.08 \times 10^{-31}$	$1.04 \pm 0.09 \times 10^{-31}$	$9.00 \pm 0.61 \times 10^{-32}$	$3.59 \pm 0.39 \times 10^{-32}$
3.20	$1.22 \pm 0.09 \times 10^{-32}$	$1.75 \pm 0.11 \times 10^{-32}$	$6.19 \pm 0.63 \times 10^{-33}$	$4.27 \pm 0.47 \times 10^{-33}$	$4.24 \pm 0.45 \times 10^{-33}$	$1.12 \pm 0.20 \times 10^{-33}$
4.00	$1.03 \pm 0.10 \times 10^{-33}$	$1.25 \pm 0.11 \times 10^{-33}$	$3.06 \pm 0.53 \times 10^{-34}$	$2.49 \pm 0.47 \times 10^{-34}$	$1.21 \pm 0.28 \times 10^{-34}$	$6.63 \pm 2.25 \times 10^{-35}$
4.80	$5.00 \pm 1.28 \times 10^{-35}$	$7.85 \pm 2.08 \times 10^{-35}$	$2.67 \pm 0.97 \times 10^{-35}$	$3.24 \pm 1.47 \times 10^{-35}$	-------------------	$5.52 \pm 5.57 \times 10^{-36}$

tion eliminated by these five cuts is 9% at a P_T of 2.4 GeV/c.

The seventh cut was on the pulse height in the last trigger counter $A4$, requiring a minimum pulse height of 50. This cut required the particle to penetrate the counter and eliminated possible contributions from particles traversing the light guide. This is shown in Fig. 8: 0.4% of the events are eliminated.

The eighth cut was on $\Delta p/p_0$, where Δp is the difference between the measured momentum and the central momentum, p_0. The cut requires that $-0.15<\Delta p/p_0<0.20$. This eliminates a small (0.2%) tail on the momentum distribution, as shown in Fig. 9. The final cut is on the position of the track at the target, as shown in Figs. 10 and 11. The target cut is also described in Table II. The calculated cross sections were stable to better than ±5% when the cuts were varied over reasonable limits.

The method described above is used to find the yield of observed particles for *high*-transverse-momentum data. In that region the essence of the problem is that the cross sections are low, and pains must be taken to eliminate sources of background. The requirements of track fitting, projection to the target and passing all the cuts accomplish this. At *low* momentum settings there are different problems. Here the high cross sections lead to high rates in the drift chambers. The low momentum leads to increased multiple scattering and more difficulty in reconstructing tracks. On the other hand, the ratio of signal to background increases to the point where background rejection is no longer significant. As a result, a different method of analysis is required.

In this case, the reconstructed events are used to obtain the relative yield of pions, kaons, protons, and muons. The number of triggers is then used without any cuts as the total observed yield. This low-momentum method is used for momentum settings of 20 GeV/c or less ($P_T<2$ GeV/c) and the high momentum method for 25 GeV/c or higher. The two methods agree to within 2% at 25 GeV/c.

The hadron identification by particle type was performed with the two precision Cherenkov counters, as in previous experiments. The upstream counter (C_A) was generally set to count pions in the outer channel (9—40 mrad Cherenkov light angle) and kaons in the inner channel (0—9 mrad). Protons were below threshold. The second counter (C_B) was set to count only pions, with both kaons and protons below threshold. Both pions and kaons are thus positively identified; protons (antiprotons) are identified by the absence of Cherenkov signals.

The efficiency of each counter was checked by comparing with the other. Any inefficiency for pions was less than 0.2%: a small inefficiency for

TABLE X. The invariant cross sections $E\,d^3\sigma/dp^3$ for the production of $\pi^\pm$, $K^\pm$, p and $\bar{p}$ at a laboratory angle of 63.7 mrad (corresponding to a laboratory angle of ~67° for relativistic particles) in 200 GeV $\pi^- p$ collisions. The units are cm^2 GeV^{-2}.

P_T (GeV/c)	π^+	π^-	K^+	K^-	p	$\bar{p}$
1.59	$1.18 \pm 0.06 \times 10^{-29}$	$1.57 \pm 0.08 \times 10^{-29}$	$3.78 \pm 0.24 \times 10^{-30}$	$3.94 \pm 0.23 \times 10^{-30}$	$3.89 \pm 0.22 \times 10^{-30}$	$2.30 \pm 0.14 \times 10^{-30}$
1.91	$2.94 \pm 0.15 \times 10^{-30}$	$4.18 \pm 0.21 \times 10^{-30}$	$1.08 \pm 0.06 \times 10^{-30}$	$9.98 \pm 0.63 \times 10^{-31}$	$9.63 \pm 0.54 \times 10^{-31}$	$5.24 \pm 0.36 \times 10^{-31}$
2.87	$6.41 \pm 0.32 \times 10^{-32}$	$9.78 \pm 0.48 \times 10^{-32}$	$2.60 \pm 0.16 \times 10^{-32}$	$2.61 \pm 0.16 \times 10^{-32}$	$1.67 \pm 0.10 \times 10^{-32}$	$9.07 \pm 0.67 \times 10^{-33}$
3.82	$2.06 \pm 0.13 \times 10^{-33}$	$3.49 \pm 0.21 \times 10^{-33}$	$9.84 \pm 0.82 \times 10^{-34}$	$9.28 \pm 0.83 \times 10^{-34}$	$4.41 \pm 0.45 \times 10^{-34}$	$1.83 \pm 0.30 \times 10^{-34}$
4.78	$1.03 \pm 0.13 \times 10^{-34}$	$2.30 \pm 0.25 \times 10^{-34}$	$3.86 \pm 0.79 \times 10^{-35}$	$2.57 \pm 0.71 \times 10^{-35}$	$1.08 \pm 0.36 \times 10^{-35}$	$3.23 \pm 2.31 \times 10^{-36}$
5.73	$4.60 \pm 1.57 \times 10^{-36}$	$1.39 \pm 0.37 \times 10^{-35}$	$1.04 \pm 0.61 \times 10^{-36}$	$1.28 \pm 0.75 \times 10^{-36}$	-------------------	$9.60 \pm 9.79 \times 10^{-37}$

kaons at low momentum due to the large momentum bite of the spectrometer is dealt with below.

Muons were found in the segmented shower counter at the end of the spectrometer by fitting to the hypothesis that the particle was minimum-ionizing. Some separation of hadrons and muons was obtained this way. The fraction of triggers which were identified as muons is given in Table III: it varies from 7.8% at $p=10$ GeV/c ($P_T \cong 0.8$ GeV/c) to 0.8% at $p=70$ GeV/c ($P_T \cong 5.6$ GeV/c). Hadrons misidentified as muons in the 8-absorption-length shower counter were estimated to be less than 10% of the muon signal, and hence always less than 1% of the yield.

All identified muons were removed from the hadron sample. Thus whether a kaon decayed upstream and the event was lost, or it decayed downstream and the muon was recorded and subsequently rejected did not matter. The kaon and pion cross sections were then corrected for decay in flight over the full length of the spectrometer up to the shower counter as described below.

B. Corrections to the yields

The yields have been corrected for particle misidentification, reconstruction inefficiency, decay in flight, absorption in the target and in the spectrometer, and the contribution of the target flask for the hydrogen data, and a correction for the finite acceptance of the spectrometer.

The particle misidentification is significant only at very low momentum. Because of the large momentum bite, 8% of kaons at 10 GeV/c ($P_T=0.8$ GeV/c), 2% at 20 GeV/c, and 1% at 25 GeV/c are below threshold. The numbers are measured directly by subdividing the measured momentum bite into finer bins. The kaon and proton data were corrected appropriately.

The yields for all particles have been multiplied by an overall factor of 1.06 ± 0.02 due to inefficiencies in the drift chambers and reconstruction program.

Decay in flight is corrected for the full length of the spectrometer, as any particle which decays before reaching the shower counter will either be lost or be identified as a muon. This procedure corrects for all muonic decay modes, i.e., all pion decays and $\frac{2}{3}$ of kaon decays, since the resulting muon will be tagged as a muon and thus removed from the hadron sample. The remaining kaons will not be accepted or be reconstructible if they decay before the second bend. The nonmuonic decays which do reconstruct are less than 2% of the total decays. The correction for pions and kaons is thus $\exp(L/\gamma c\tau)$, where $L=258$ ft is the length of the spectrometer and $\gamma c\tau$ is the lifetime in ft in the laboratory. The correction factor ranges from 1.15 and 2.84 for pions and kaons (respectively) at 10 GeV/c to 1.02 and 1.16 at 70 GeV/c.

The correction for absorption in the scintillator and Cherenkov windows in the spectrometer is done separately for each particle species and sign using the absorption cross sections of Ref. 15. The material in the spectrometer excluding Cherenkov gas amounted to 0.12 absorption lengths; the corresponding corrections are 9% for π^+, π^-, and K^-, 8% for K^+, and 12% and 13%, respectively, for protons and antiprotons.

The correction for absorption in the gas in the

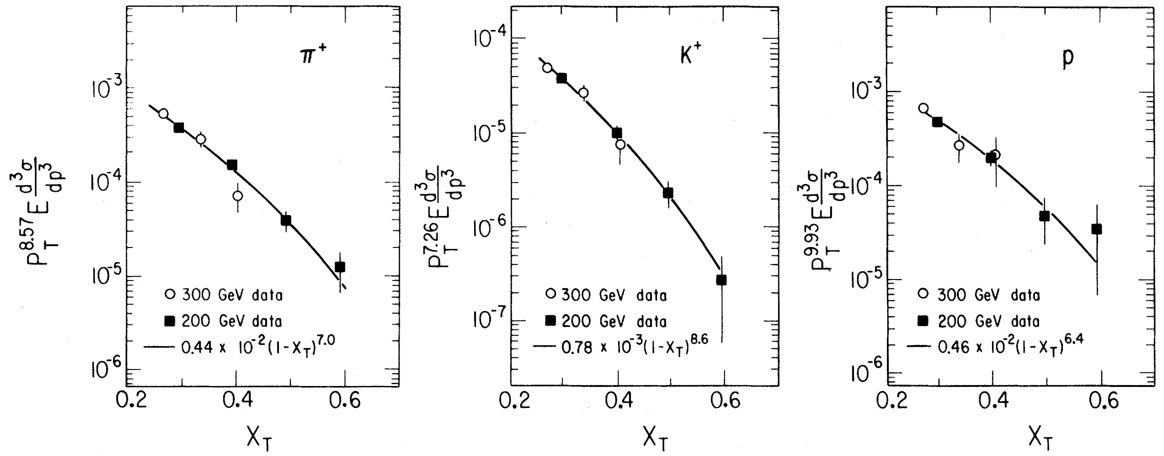

FIG. 13. The scaling of the cross sections for the positive particles π^+, K^+, and protons versus $x_T=2P_T/\sqrt{s}$. Each data point has been multiplied by $P_T{}^n$, where P_T is the P_T value for that point, and n is the best-fit value from the parametrization.

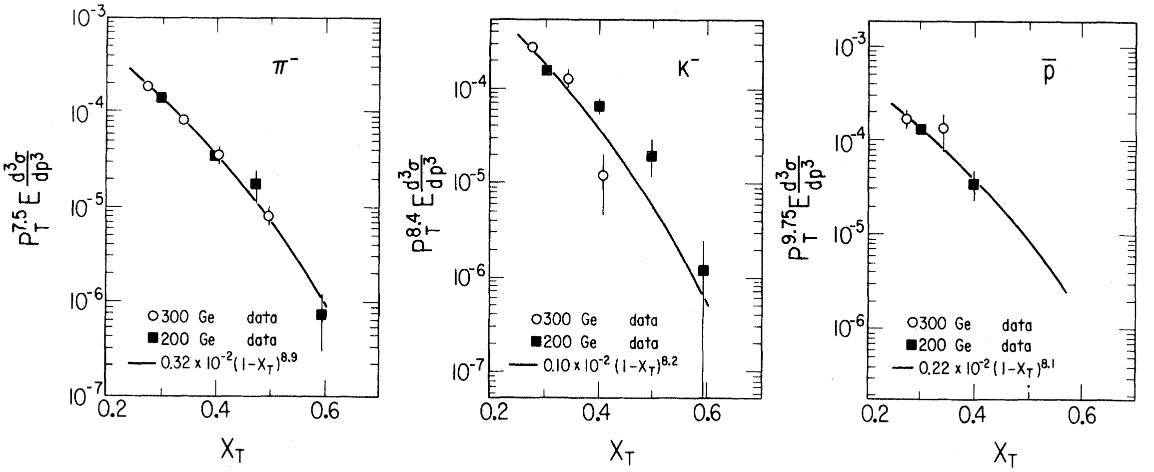

FIG. 14. The scaling of the cross sections for the negative particles π^-, K^-, and $\bar{p}$ versus $x_T = 2P_T/\sqrt{s}$. Each data point has been multiplied by $P_T{}^n$, where P_T is the P_T value for that point, and n is the best-fit value from the parametrization.

Cherenkov counters is greater than a few percent only at momenta of 10 or 15 GeV/*c* ($p_T = 0.8$ or 1.2 GeV/*c*). The worst case is an 11% correction at $p = 10$ GeV/*c* ($p_T \sim 0.8$ GeV/*c*). Separate runs with the Cherenkov counters empty checked these corrections.

For the hydrogen data a correction was required for the effect of the target flask. This correction was measured at each momentum setting with empty target runs. The correction, which was on the order of 10%, depended weakly on momentum and particle type (due to the A dependence of high-P_T cross sections), and the incoming-particle type. For pions, for example, the correction ranged from 8 to 12% over the momentum range from 10 to 70 GeV/*c*.

The final correction required was due to the large momentum bite of the spectrometer and the rapidly falling spectrum with P_T. These resulted in the average P_T of accepted events lying lower than the central momentum of the spectrometer.

To correct for this, either by correcting the yield itself as was done, or equivalently by altering the P_T scale, one has to know the acceptance of the spectrometer versus momentum quite accurately. This was accomplished by simple Monte Carlo techniques, and checked by measuring the same momentum interval of the spectrum in different parts of the momentum-bite acceptance. Three runs were taken, at spectrometer settings 25, 27.5, and 30 GeV/*c*. Because the momentum acceptance is approximately 20%, these runs have a large overlap in momentum. The corrected data agree well over the full acceptance, giving us confidence in the acceptance calculations.

The acceptance correction was an iterative procedure. A cross section was calculated for each P_T using an average acceptance. A local slope in P_T was then calculated for each data point. This slope was used to correct the data point for the effect of the fall of the spectrum across the acceptance. The procedure was iterated and converged rapidly, with most cross sections changing by less than 1% after the second iteration.

The acceptance corrections are large because the P_T spectra are steep. A typical correction is 25% for pions at $P_T = 3$ GeV/*c*; the largest corrections are 50% at $P_T = 6$ GeV/*c*. The corrections, however, are well known as they depend only on the local slope, and less strongly on the details of the acceptance. The estimated error on this slope correction

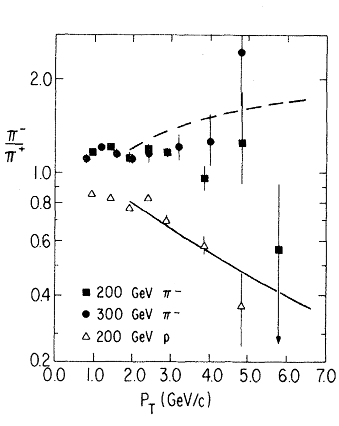

FIG. 15. The π^-/π^+ ratio versus P_T in 200 and 300 GeV $\pi^- p$ collisions. The same ratio measured in 200 GeV pp collisions is shown for comparison. The lines are the prediction of Field (Ref. 23).

is 2% at a $P_T = 2$ GeV/c; although it increases with P_T, it is always less than the statistical error at large P_T.

C. Normalization of the incoming beam (N_b)

Both the pion and proton beams were normalized with the ion chambers directly upstream of the target. Values from Ref. 16 for dE/dx and the average energy per pair were used. The resulting normalization was checked radiochemically[17] using the reactions $p + \mathrm{Cu} \rightarrow {}^{24}\mathrm{Na} + X$ and $\pi^- + \mathrm{Cu} \rightarrow {}^{57}\mathrm{Co} + X$ induced in foils inserted into the beam, as well as by direct counting at reduced intensity using a scintillator target viewed by the 90° monitors. All four methods agree to within 10%.

D. The momentum scale

The momentum scale of the spectrometer was determined by the value of the magnetic field in the second dipole, and by the surveyed bend angles of the spectrometer. The magnet current was monitored directly from the shunt on the power supply, and was known to better than 0.2%. The scale was checked in an absolute fashion by means of the Cherenkov counters. Two smaller counters $A5$ and $A6$ (see Fig. 4) at the downstream focus were used to select a small momentum bite around the central momentum, which was set to 27.5 GeV/c. The Cherenkov counters were then stepped in pressure past the kaon threshold. Knowing precisely the index of refraction which gives a Cherenkov angle of 9 mrad allows a measurement of β for kaons, and hence the momentum. The two counters gave values of 27.3 ± 0.2 and 27.5 ± 0.2 GeV/c for a nominal magnet setting of 27.5 GeV. We conclude that the momentum scale is known to 0.7%.

E. Angular measurements

The angle between the unpitched beam and the spectrometer was 80 mrad. This number was obtained by surveying the spectrometer and is known to an accuracy of about 0.3% (its accuracy is limited by the uncertainty in the direction of the incident beam).

When the beam was pitched to the East or West to change the production angle (see Fig. 2) the angles determined from the SWIC in front of the target (and checked by the known transfer constants of the pitching magnets) were 63.7 ± 0.6 and 96.3 ± 0.6 mrad, respectively.

F. Discussion of errors

At the low-momentum region (10, 15, and 20 GeV/c) the errors in the cross sections are dominated by systematic uncertainties. There follows a transition region (~ 30 GeV/c) where systematic and statistical errors are about equal. Finally, at high momenta (≥ 40 GeV/c) the statistical errors are dominant.

At low momenta (10, 15, and 20 GeV/c) we assigned a systematic error of $\pm 8\%$, estimated from the agreement between the cross sections computed by the low momentum and full reconstruction methods. All other systematic errors are much smaller in this low momentum region and were neglected (for example, the maximum error in the empty-target subtraction from the hydrogen target is $\pm 2\%$, the maximum error because of muon misidentification is $\sim \pm 2\%$, the maximum error in the slope correction is $\sim \pm 1\%$, the maximum error because of absorption is $\sim \pm 2\%$). The total error quoted in the cross sections in this momentum region is the statistical error plus the $\pm 8\%$ systematic error added in quadrature.

For momenta greater than 25 GeV/c, the total error is the sum of the following errors: the error in the slope correction, the error in the empty-target subtraction ($\pm 2\%$, for the hydrogen target only), the error because of beam motion and the uncertainty in the acceptance ($\pm 4\%$), the error in the target absorption correction ($\pm 2\%$ for nuclear targets only), and the statistical error. These errors were added in quadrature.

Not included in the errors quoted on the cross sections is a $\pm 12\%$ overall normalization error. It is the sum in quadrature of the uncertainty in the beam normalization ($\pm 10\%$), the uncertainty in the reconstruction program inefficiency ($\pm 2\%$), the error in the cross section because of the uncertainty in the transverse-momentum scale ($\pm 5\%$) and the overall uncertainty in the integrated acceptance ($\pm 5\%$).

IV. THE PRODUCTION OF $\pi^{\pm}$, $K^{\pm}$, p, AND $\bar{p}$ IN $\pi^- p$ COLLISIONS

A. The energy and P_T dependence of the cross sections

In this section we present the cross sections measured with the liquid hydrogen target. Two beam energies, 200 and 300 GeV, were used in order to extract the dependence of the cross section on the total c.m. energy $\sqrt{s}$ and on the transverse momentum P_T. This represents the first time that these dependences have been measured for *charged*-single-hadron production in $\pi^- p$ collisions.

The invariant cross sections $E\,d^3\sigma/dp^3$ for the production of $\pi^\pm$, $K^\pm$, p and $\bar{p}$ at a laboratory angle of 96.3 mrad (c.m. angle ~90°) in 200 GeV π^-p collisions are given in Table IV. The 300 GeV cross sections, also measured at a laboratory angle corresponding to 90° in the π^-p c.m. frame, are given in Table V. These 200 and 300 GeV data for π^+ and π^- production at 90° are shown in Figure 12 as darkened circles and triangles, respectively.

We have fitted our data for the production of π^+, π^-, K^+, K^-, p, and $\bar{p}$'s each to the form

$$E\,d^3\sigma/dp^3 = C(1/P_T)^n(1-x_T)^b\ .$$

This functional form corresponds to the overly simple prediction of dimensional counting[18] for a *single* scattering subprocess (e.g., single-gluon exchange[19] gives $n=4$ and $b=7$ for π^-p scattering), but it provides a convenient parametrization, and in general is a good fit to all existing data. In pp collisions at these energies and transverse momenta, n is observed[8] to have values close to 8, rather than 4. At higher values of $\sqrt{s}$ ($\sqrt{s} > 50$ GeV) and appreciably higher values of P_T ($P_T \geq 10$ GeV/c) the value of n obtained is observed to drop[20] to values near 6 in inclusive π^0 production in pp collisions.

The one previous measurement[21] of n in π^-p high-P_T collisions was obtained in a comparison of the production of π^0's at 100 and 200 GeV. The value obtained for n in $\pi^-p \rightarrow \pi^0 + X$ was 10.0, basically in agreement with the value of 10.8 measured by the same experiment in $pp \rightarrow \pi^0 + X$. This value for n in pp collisions is in good agreement with the extrapolation of *charged-pion* production[8] to 100 GeV.

The fits have been performed over the region $P_T > 2.6$ GeV/c. The fit quality and the values for the fitted parameters are insensitive to increasing this cutoff value of P_T. Decreasing the cutoff causes the values to change, indicating significant contributions from the low-P_T processes with little energy dependence.

The resulting χ^2's and best-fit values of the parameters n and b are given in Table VI. The fits are all acceptable except for that of the K^-, which has one point which is several standard deviations away from a good fit.

In Figs. 13 and 14 we show the data after multiplication by $P_T{}^n$, where n is the best-fit power. The 200 and 300 GeV data lie on a single curve in x_T, showing that this form of scaling is a good representation of the data.

The results of the fits show that n is approximately 8 for the production of $\pi^\pm$ and $K^\pm$, and is close to 10 for the production of p and $\bar{p}$. The values found experimentally[8] for n in the pp case are also

TABLE XI. The measured π^-/π^+, K^-/K^+, and $\bar{p}/p$ ratios versus P_T in 200 GeV π^-p collisions for each of the three laboratory angles.

	96.3 mrad (lab angle)				80 mrad (lab angle)				63.7 mrad (lab angle)		
P_T (GeV/c)	π^-/π^+	K^-/K^+	$\bar{p}/p$	P_T (GeV/c)	π^-/π^+	K^-/K^+	$\bar{p}/p$	P_T (GeV/c)	π^-/π^+	K^-/K^+	$\bar{p}/p$
0.96	1.17 ± 0.02	0.75 ± 0.05	0.39 ± 0.02								
1.44	1.21 ± 0.02	0.78 ± 0.03	0.41 ± 0.01								
1.93	1.12 ± 0.04	0.76 ± 0.06	0.42 ± 0.03					1.59	1.33 ± 0.04	1.04 ± 0.06	0.59 ± 0.03
2.41	1.19 ± 0.02	0.75 ± 0.03	0.31 ± 0.01	2.40	1.29 ± 0.06	0.84 ± 0.07	0.40 ± 0.04	1.91	1.42 ± 0.04	0.92 ± 0.05	0.54 ± 0.03
2.89	1.16 ± 0.04	0.68 ± 0.06	0.33 ± 0.03	3.20	1.44 ± 0.11	0.69 ± 0.09	0.26 ± 0.05	2.87	1.53 ± 0.05	1.01 ± 0.06	0.54 ± 0.04
3.85	0.96 ± 0.09	0.67 ± 0.13	0.24 ± 0.08	4.00	1.21 ± 0.14	0.82 ± 0.20	0.55 ± 0.22	3.82	1.70 ± 0.10	0.94 ± 0.10	0.42 ± 0.08
4.82	1.25 ± 0.33	0.64 ± 0.31	-----------	4.80	1.57 ± 0.57	1.21 ± 0.70	-----------	4.78	2.24 ± 0.35	0.67 ± 0.22	0.30 ± 0.23
5.78	0.56 ± 0.36	0.63 ± 0.78	-----------					5.73	3.02 ± 1.29	1.23 ± 1.02	-----------

shown in Table VI; in *pp* collisions *n* is also consistent with 8 for π^+, π^-, K^+ and perhaps K^- and $\bar{p}$'s, but the value of *n* for protons is approximately 12, and seems higher than the value for $\bar{p}$'s.

If the fundamental scattering process producing the high-P_T secondaries is the same in π^-p and *pp* collisions, one would expect the fitted values of *n* to be the same. For such processes, dimensional counting would predict that the value of *b* should be two units less, as there is one fewer spectator quark in the π^-p collision. For K^- and $\bar{p}$ production in particular, however, the presence of the valence antiquark in the π^-p collisions means that different scattering processes may contribute in the π^-p and *pp* cases, and *n* and *b* would be quite different.

Comparing the fitted values for *n* and *b* in Table VI for the two different beams, we see that indeed the values of *b* for $\bar{p}$'s and K^- are quite different in the two cases, but otherwise the value of *b* in π^-p collisions tends to be only slightly smaller than in *pp* collisions. The values for *n* are very similar in all cases.

B. The relative production of $\pi^\pm$, $K^\pm$, *p*, and $\bar{p}$ in π^-p collisions

In this section we consider the ratios of the various particle types produced in π^-p collisions. The quantum numbers of the particles reflect those of the incoming constituents.[22] An example of this is seen in the proton-proton scattering case[8]: the ratio of π^+ to π^- climbs at large x_T, reflecting the dominance of the *u* quarks in the proton. Another example, again from the *pp* case, is that the ratio of K^+/π^+ is constant at about 0.5, reflecting that in both cases a *u* quark is scattered out, and that picking up an $\bar{s}$ out of the sea is only about one-half as probable as picking up a $\bar{d}$.

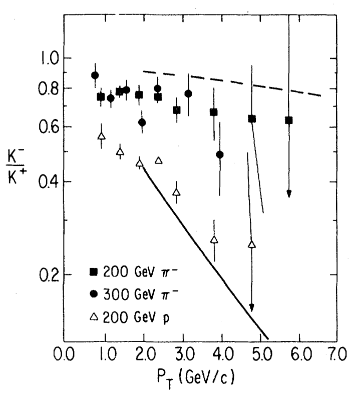

FIG. 16. The K^-/K^+ ratio versus P_T in 200 and 300 GeV π^-p collisions. The same ratio measured in 200 GeV *pp* collisions is shown for comparison. The lines are the prediction of Field (Ref. 23).

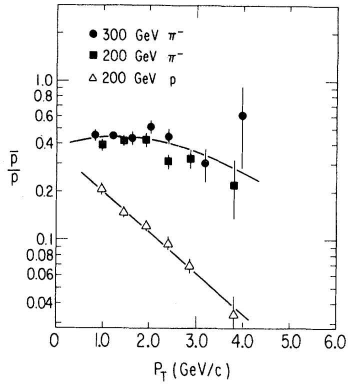

FIG. 17. The $\bar{p}/p$ ratio versus P_T in 200 and 300 GeV π^-p collisions. The same ratio measured in 200 GeV *pp* collisions is shown for comparison. The solid lines are merely to guide the eye.

In π^-p scattering the presence of the $\bar{u}$ quark changes some of the particle-production ratios. The three antiparticle/particle ratios, the π^-/π^+, K^-/K^+, and $\bar{p}/p$ are shown in Table VII. Also given are the ratios K^+/π^+, p/π^+, K^-/π^-, and $\bar{p}/\pi^-$. Ratios measured in 200 GeV *pp* collisions are included in this table—they agree well with the more extensive measurements of Ref. 8.

Figure 15 shows the ratio of π^- to π^+ produced in 200 and 300 GeV π^-p collisions versus p_T. The π^-/π^+ ratio is essentially flat in P_T. Predictions of a QCD model[23] are shown. The predictions of a constituent-interchange model[24] (CIM) are off scale on this plot. In contrast, the π^-/π^+ ratio measured in *pp* collisions falls with P_T, as also indicated in Fig. 15. In Figs. 16 and 17 ratios are presented. In both cases the ratios are much larger than in the corresponding *pp* case, and fall much more slowly with P_T.

The heavy-particle compositions are presented in Figs. 18 and 19. In these figures are plotted the ratios K^+/π^+, p/π^+, K^-/π^-, and $\bar{p}/\pi^-$ for 200 GeV π^-p collisions.

The K^+/π^+ ratio in π^-p collisions is indistinguishable from the ratio in *pp* collisions. It levels off at a value of approximately 0.5. This value is consistent with the value expected from the SU(3) breaking of the sea.[25] The simplest mechanism is that both a π^+ and a K^+ contain a *u* quark (*u*); whether one gets a π^+ or a K^+ depends only on whether the *u* quark picks up a $\bar{d}$ or an $\bar{s}$ antiquark on the way out.

The p/π^+ ratio is similar in shape in π^-p collisions to the ratio in *pp* collisions, but is approximately half the value. This is consistent with a model in which most of the secondary protons come from a primary proton. (The proton production in *pp* collisions has always been higher than most

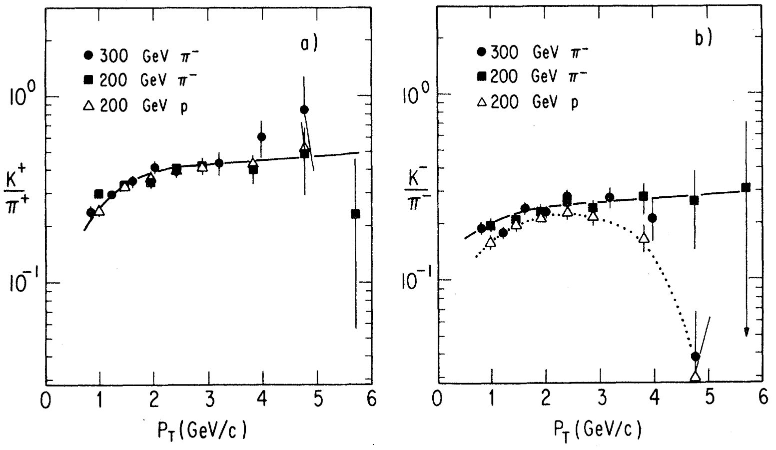

FIG. 18. (a) The ratio of produced K^+/π^+ versus P_T in 200 and 300 GeV π^-p collisions. The same ratio measured in 200 GeV *pp* collisions is shown for comparison. (b) The similar plot for the K^-/π^- ratio.

hard-scattering models predicted.)

The K^-/π^- ratio is appreciably flatter in P_T for π^-p collisions than for *pp* collisions. This is not unexpected as the K^- contains a $\bar{u}$ antiquark which is a valence antiquark of the pion. One would expect this ratio to be flat in simple quark counting.

The $\bar{p}/\pi^-$ ratio in π^-p collisions is in fact not much different in shape from the $\bar{p}/\pi^-$ ratio in *pp* collisions, but is enhanced by a factor of two.

C. The angular dependence of the π^-p cross sections

The magnets upstream of the target (see Fig. 2) were installed to change the beam angle such that cross sections could be measured at an angle corresponding to 90° in the c.m. frame at 200 as well as at 300 GeV. The exact angle in the c.m. of course depends on the velocity of the produced particle. The angles in the center of mass for each of the particle types are tabulated in Table VIII for each momentum at which data were taken.

Unlike the proton-proton case, in π^-p scattering the angular distribution need not be symmetric about 90°. The production of hadrons into the pion hemisphere, for example, will reflect the constituent structure and fragmentation functions in the pion more than those of the proton. In the proton hemisphere the characteristics of the proton constituents

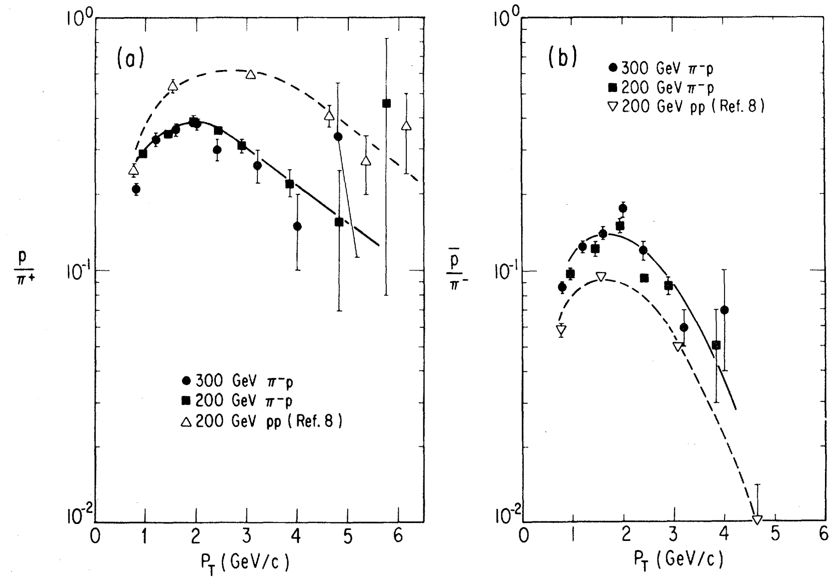

FIG. 19. (a) The ratio of produced p/π^+ versus P_T in 200 GeV and 300 GeV π^-p collisions. The same ratio measured in 200 GeV *pp* collisions is shown for comparison. (b) The similar plot for the $\bar{p}/\pi^-$ ratio.

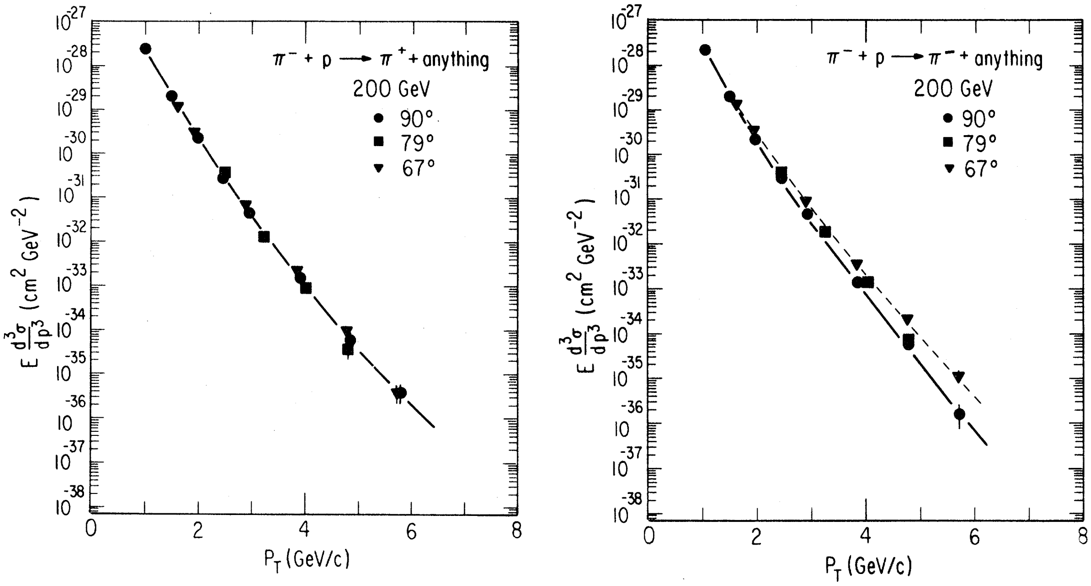

FIG. 20. The invariant cross section $E\,d^3\sigma/dp^3$ versus P_T for the production of π^+ and π^-. Data at three different laboratory angles, $\theta_{\text{lab}}=96.3$, 80, and 63.7 mrad, are presented. These correspond, respectively, to c.m. angles of $\theta=90°$, 79°, and 67° for relativistic particles.

will be more dominant.

As the cross sections are steep in p_T, the measurement of a single particle predominantly samples those decays in which a single particle carries away most of the quark momentum, and hence reflects the direction of the constituent as well. The measured angular dependence should thus be strongly correlated with the angular dependence of the underlying hard-scattering process.

The cross sections for the production of single hadrons in 200 GeV $\pi^- p$ collisions at laboratory angles of 80 mrad (c.m. angle$\sim$79°) and 63.7 mrad (c.m. angle $\sim$67°) are given in Tables IX and X, respectively. Figure 20 shows the π^- and π^+ cross sections at these angles as well as at $\theta_{\text{lab}}=96.3$ mrad ($\theta_{\text{c.m.}} \simeq 90°$). The cross sections for kaons and protons (antiprotons) at the three angles are shown in Figs. 21 and 22. It is clear from these last three fig-

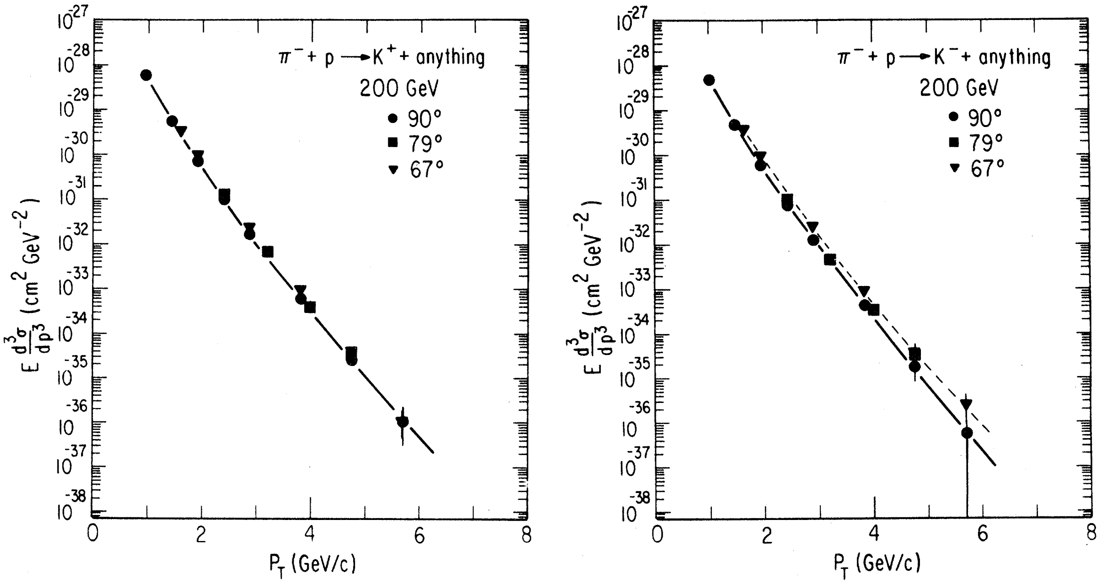

FIG. 21. The invariant cross section $E\,d^3\sigma/dp^3$ versus P_T for the production of K^+ and K^-. Data at three different laboratory angles, $\theta_{\text{lab}}=96.3$, 80, and 63.7 mrad, are presented. These correspond respectively to c.m. angles of $\theta=90°$, 79°, and 67° for relativistic particles.

TABLE XII. The measured K^+/π^+ and K^-/π^- ratios versus P_T in 200 GeV π^-p collisions for each of the three laboratory angles.

96.3 mrad (lab angle)			80 mrad (lab angle)			63.7 mrad (lab angle)		
P_T (GeV/c)	K^+/π^+	K^-/π^-	P_T (GeV/c)	K^+/π^+	K^-/π^-	P_T (GeV/c)	K_+/π^+	K^-/π^-
0.96	0.30 ± 0.01	0.19 ± 0.01						
1.44	0.32 ± 0.01	0.21 ± 0.01						
1.93	0.34 ± 0.02	0.23 ± 0.02				1.59	0.32 ± 0.02	0.25 ± 0.01
2.41	0.41 ± 0.01	0.26 ± 0.01	2.40	0.43 ± 0.03	0.28 ± 0.02	1.91	0.37 ± 0.02	0.24 ± 0.01
2.89	0.41 ± 0.02	0.24 ± 0.02	3.20	0.51 ± 0.06	0.24 ± 0.03	2.87	0.41 ± 0.02	0.27 ± 0.01
3.85	0.40 ± 0.06	0.28 ± 0.05	4.00	0.30 ± 0.06	0.20 ± 0.04	3.82	0.48 ± 0.04	0.27 ± 0.02
4.82	0.51 ± 0.18	0.26 ± 0.10	4.80	0.54 ± 0.24	0.41 ± 0.22	4.78	0.38 ± 0.09	0.11 ± 0.03
5.78	0.27 ± 0.22	0.30 ± 0.34				5.73	0.23 ± 0.15	0.09 ± 0.06

ures that the angular dependence of the negative particles is stronger than that of the positive particles in this angular region.

Figure 23 shows the values of the π^-/π^+, K^-/K^+, and $\bar{p}/p$ ratios versus p_T for the three angles. The increase in the production of negatively charged particles as the c.m. angle decreases is shown. The predictions of Ref. 23 are also shown for the π^-/π^+ and K^-/K^+ ratios. The numerical values of these ratios are given in Table XI.

Figure 24 shows the K^+/π^+ and K^-/π^- ratios versus p_T. Figure 25 shows the analogous p/π^+ and $\bar{p}/\pi^-$ ratios. These are listed in Tables XII and XIII, respectively.

Finally, Fig. 26 presents the π^-/π^+, K^-/K^+, and K^-/π^- ratios measured at $p_T \approx 4$ GeV/c versus $\theta_{\text{c.m.}}$.[26] The value measured in pp collisions at 90° is shown for comparison, as are the predictions of Ref. 23. For the π^-/π^+ ratio, a later modification of the parameters of the model, in which the gluon fragmentation was made harder, clearly fits the data better.

D. The comparison of single-particle cross sections in π^-p and pp collisions

It is well known that the πp total cross section is very close to $\frac{2}{3}$ of the value of the pp cross section.[27] At low values of p_T the multiplicities are not so different, so that one would expect the πp cross section for the inclusive production of single particles to be about $\frac{2}{3}$ of the pp cross section. Figure 27 shows the ratio of the π^-p invariant cross section to the pp invariant cross section for pion production versus P_T. The average of the π^+ and π^- cross sections has been plotted so that a comparison can be made

TABLE XIII. The measured p/π^- and $\bar{p}/\pi^-$ ratios versus P_T in 200 GeV π^-p collisions for each of the three laboratory angles.

96.3 mrad (lab angle)			80 mrad (lab angle)			63.7 mrad (lab angle)		
P_T (GeV/c)	p/π^+	$\bar{p}/\pi^-$	P_T (GeV/c)	p/π^+	$\bar{p}/\pi^-$	P_T (GeV/c)	p/π^+	$\bar{p}/\pi^-$
0.96	0.29 ± 0.01	0.098 ± 0.004						
1.44	0.35 ± 0.01	0.122 ± 0.008						
1.93	0.39 ± 0.02	0.15 ± 0.01				1.59	0.33 ± 0.01	0.146 ± 0.007
2.41	0.36 ± 0.01	0.094 ± 0.004	2.40	0.31 ± 0.02	0.10 ± 0.01	1.91	0.33 ± 0.01	0.125 ± 0.007
2.89	0.31 ± 0.02	0.087 ± 0.008	3.20	0.35 ± 0.04	0.06 ± 0.01	2.87	0.26 ± 0.01	0.093 ± 0.006
3.85	0.22 ± 0.03	0.05 ± 0.02	4.00	0.12 ± 0.03	0.05 ± 0.02	3.82	0.21 ± 0.02	0.05 ± 0.01
4.82	0.16 ± 0.09	-------------	4.82	-----------	0.07 ± 0.07	4.78	0.10 ± 0.04	0.014 ± 0.01
5.78	0.46 ± 0.37	-------------				5.73	-----------	0.07 ± 0.07

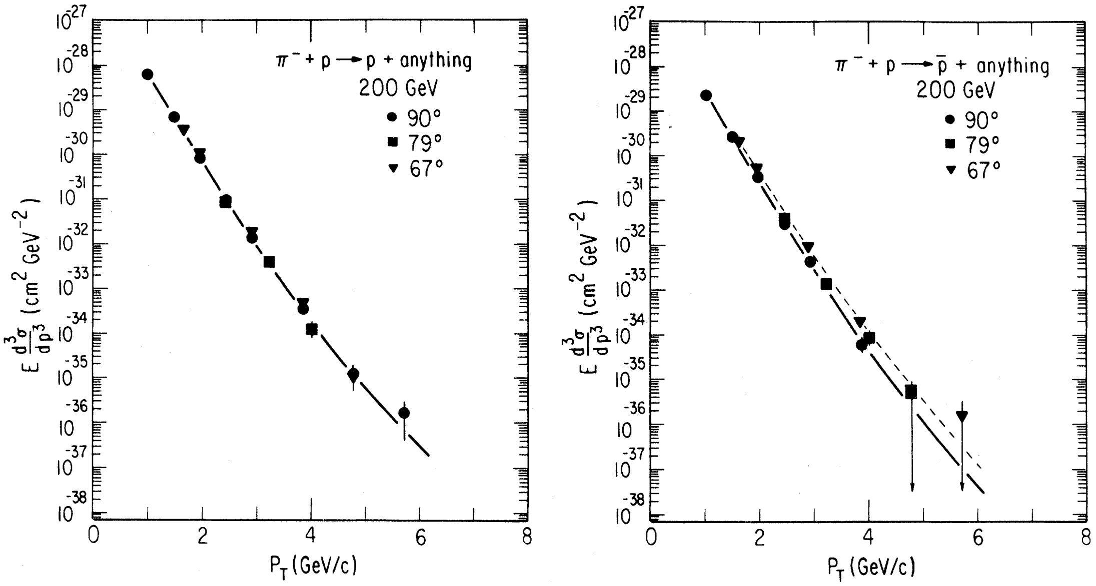

FIG. 22. The invariant cross section $E\,d^3\sigma/dp^3$ versus P_T for the production of p and $\bar{p}$. Data at three different laboratory angles, $\theta_{\text{lab}} = 96.3$, 80, and 63.7 mrad, are presented. These correspond respectively to c.m. angles of $\theta = 90°$, 79°, and 67° for relativistic particles.

with the π^0 data of Donaldson *et al.*[5] The ratio of pion production by pions to that by protons is seen to grow smoothly from a value of about $\frac{2}{3}$ for $P_T < 2$ GeV/c to almost 2 at $P_T \sim 5$ GeV/c. The individual beam ratios

$$\frac{E\,d^3\sigma/dp^3(\pi^- p \to \pi^+ + X)}{E\,d^3\sigma/dp^3(pp \to \pi^+ + X)}$$

and

$$\frac{E\,d^3\sigma/dp^3(\pi^- p \to \pi^- + X)}{E\,d^3\sigma/dp^3(pp \to \pi^- + X)}$$

are plotted versus P_T in Fig. 28. At low values of P_T protons are more effective than π^- at producing both π^- and π^+ secondaries, as could be expected from the total cross sections. At large values of P_T, π^- are much more effective than protons in producing π^-, and are at least equal to protons in producing π^+.

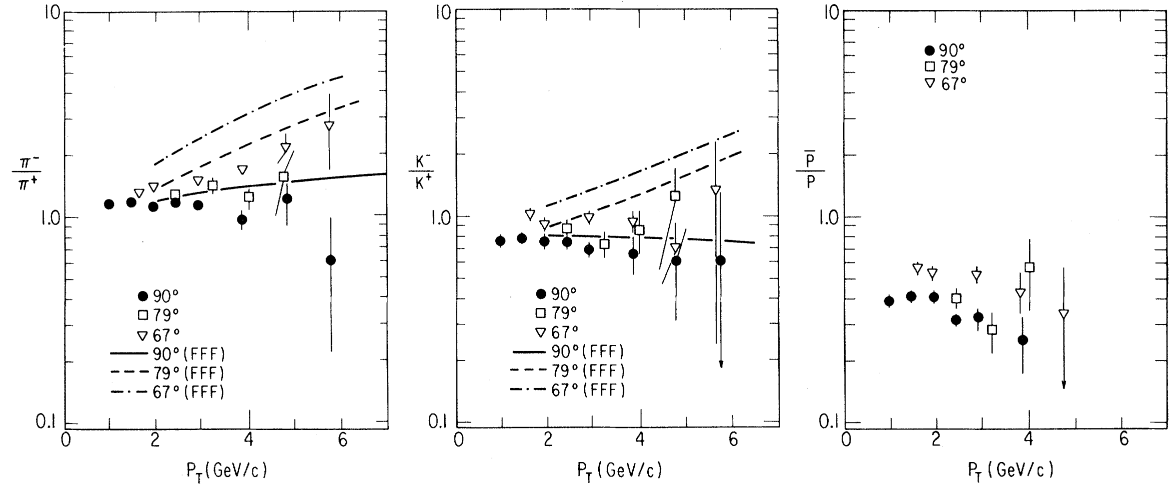

FIG. 23. The values of antiparticle/particle production ratios at different angles versus P_T. Also shown are the predictions of Ref. 23 for the meson ratios (no predictions exist for the $\bar{p}/p$ ratio).

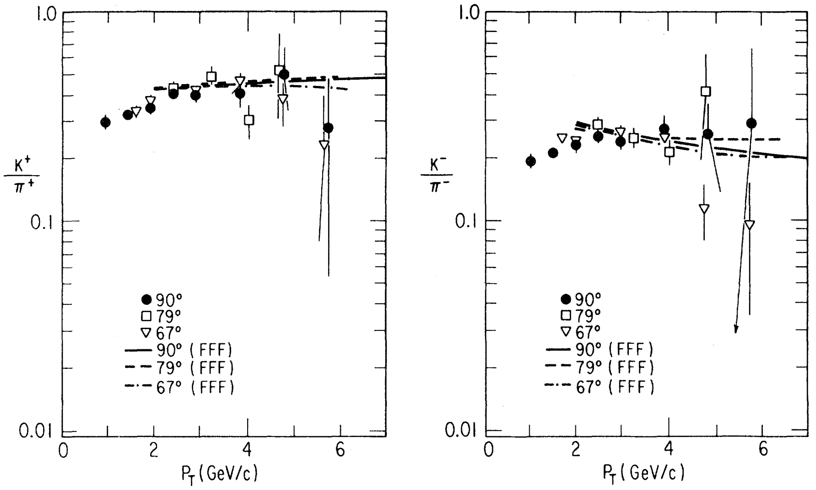

FIG. 24. The ratios of produced K^+ to π^+ and K^- to π^- versus P_T for the three production angles.

Two mechanisms are probably involved in this effect. The first is that the π^- has constituents with higher average momenta than does a proton. The second, which is relevant only to π^- production, is that the initial π^- clearly has the right ingredients to make another π^-, whether by a valence-quark scatter or a process which involves both quarks.

The "beam ratio" for K^+ and K^- production is shown in Fig. 29. K^- are produced three times more copiously by π^- than by protons at a P_T of ~4 GeV/*c*. K^+ production rises to be at least equal in $\pi^- p$ and pp collisions.

The beam ratios for p and $\bar{p}$ productions are shown versus P_T in Fig. 30. Antiproton production is strongly enhanced in $\pi^- p$ collisions over pp collisions in a fashion very much like the K^- production of Fig. 29.

Proton production in $\pi^- p$ collisions, however, is a little less than half that of pp collisions at all values of p_T. Proton production in pp collisions at these energies has always seemed anomalously large, with more protons produced at large P_T than pions.[8] It is interesting that replacing one of the two colliding protons with a π^- reduces the proton production by approximately one half.

The beam ratios for the six particle types are tab-

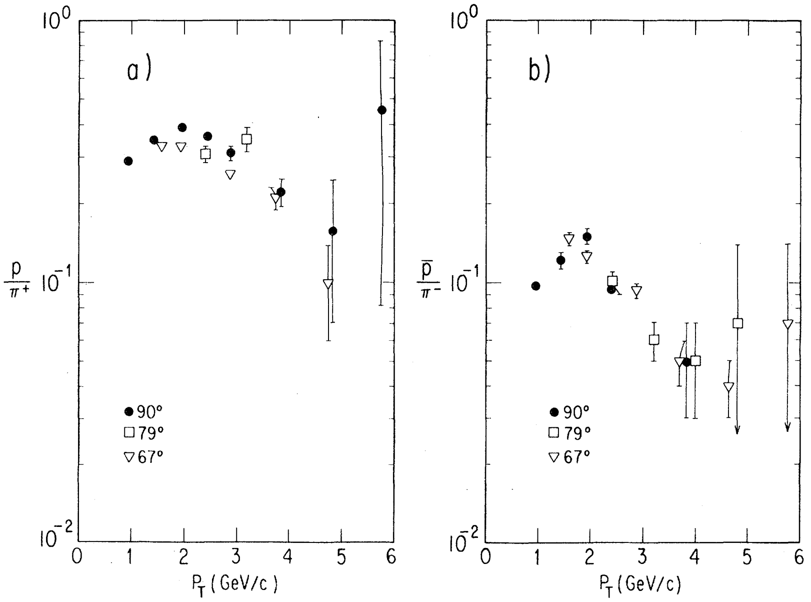

FIG. 25. The ratios of produced protons to π^+ and $\bar{p}$'s to π^- versus P_T for the three production angles.

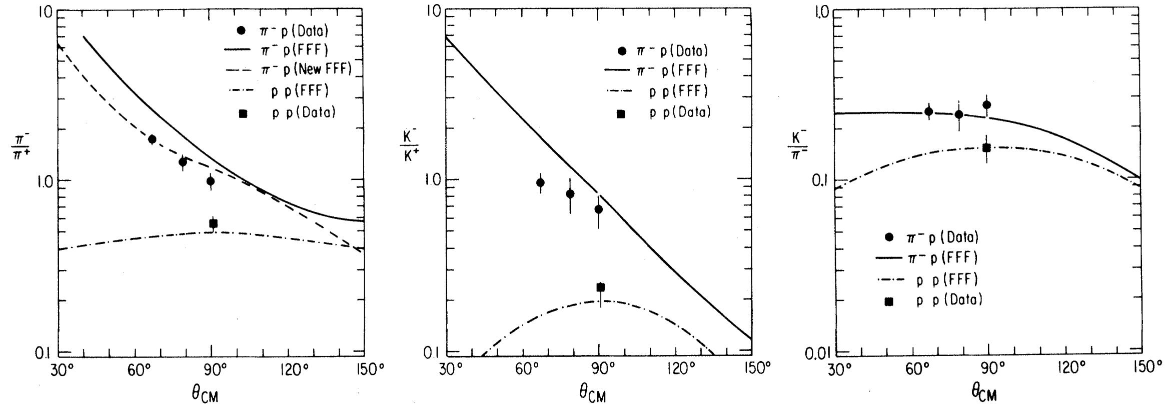

FIG. 26. The antiparticle-particle ratios measured at $P_T=4$ GeV versus $\theta_{\text{c.m.}}$. Also shown are the predictions of Ref. 23.

ulated versus P_T in Table XIV.

V. ATOMIC-WEIGHT DEPENDENCE IN $\pi^- N$ COLLISIONS

In addition to the $\pi^- p$ data described in Sec. IV, some data were taken with nuclear targets. Three nuclear targets of quite different atomic weights, beryllium (Be), copper (Cu), and tungsten (W), were used. Data were taken at 200 and 300 GeV, at laboratory angles corresponding to approximately 90° in the pion—single-nucleon c.m. frame. The most complete set of data on all three targets was taken at 200 GeV; at 300 GeV data were taken only on the W target.

The targets are described in Sec. II and Table I. All three nuclear targets were approximately 40% of an interaction length. A much shorter (4% absorption length) Be target was used to check that secondary scattering effects were negligible. The agreement between the cross sections measured on the long and the short Be targets was better than 5%.

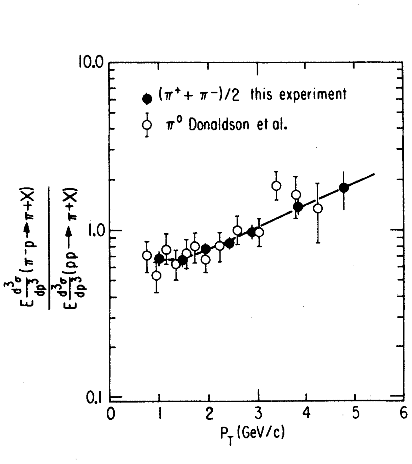

FIG. 27. The ratio of the $\pi^- p$ invariant cross section for the production of pions in $\pi^- p$ collisions to the cross sections in pp collisions, versus P_T. The data of Donaldson *et al.* (Ref. 21) have also been plotted for comparison.

The 200 GeV data on $\pi^-\text{Be} \to h + X$ are presented versus P_T in Table XV. In Table XVI the data on the Cu target are presented. The data with the best statistics, on $\pi^-\text{W} \to h + X$, are given in Table XVII for 200 GeV π^-, and in Table XVIII for 300 GeV π^-.

The cross sections for the production of the six particle types $\pi^\pm$, $K^\pm$, p, and $\bar{p}$ are shown versus P_T for the W and Be targets in Fig. 31.

The data have been parametrized by the form

$$E\frac{d^3\sigma}{dp^3}(A)=CA^{\alpha_i} ,$$

where C is a constant, A is the atomic weight of the

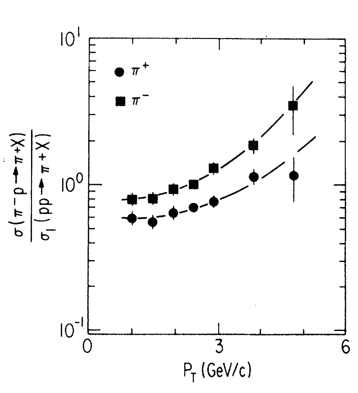

FIG. 28. The ratios of invariant cross sections for π^+ and π^- production in 200 GeV $\pi^- p$ collisions to those in pp collisions, versus P_T. The lines are only to guide the eye.

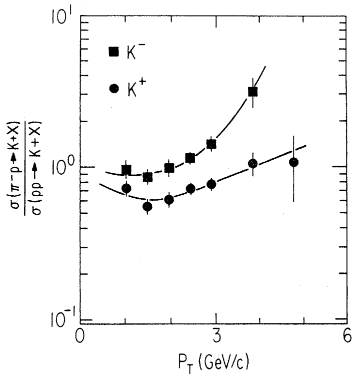

FIG. 29. The ratios of invariant cross sections for K^+ and K^- production in 200 GeV $\pi^- p$ collisions to those in pp collisions, versus P_T. The lines are only to guide the eye.

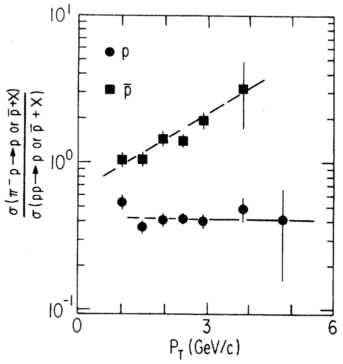

FIG. 30. The ratios of invariant cross sections for p and $\bar{p}$ production in 200 GeV $\pi^- p$ collisions to those in pp collisions, versus p_T. The lines are only to guide the eye.

target nucleus, and α_i is the parameter which measures the effective power-law dependence for the particle type i ($i = \pi^\pm, K^\pm, p, \bar{p}$). Such a parametrization is purely descriptive: parametrizations with deeper motivations[28–31] such as

$$\alpha_i = a_i A^{2/3} + b_i A^1 + c_i A^{4/3}$$

give fits which are indistinguishable from the simple one-parameter A^{α_i} form. The data are presented in tabular form so that anybody can fit a preferred form. As we claim little real understanding of the obviously complicated mechanisms behind these data, no effort has been spent in correcting for the small A/Z ratio differences in the nuclei.

Figure 32 shows the data and the A^{α_i} parametrizations for $P_T = 2.9$ GeV/c. The H, Be, and Cu cross sections relative to the W cross section versus the logarithm of the atomic weight have been plotted for each of the particle types. The hydrogen target ($\pi^- p$) data are shown only for comparison on the same plot; they are not included in any of the A-dependence fits.

The values of α_i derived from these fits are shown versus P_T in Fig. 33, and are tabulated in Table XIX. Also shown in Fig. 33 are the values obtained in pN collisions from Ref. 8 at a laboratory angle of 80° mrad (~79° in the c.m.).

From Fig. 33 we see that the values of α_i for the π^- beam are very similar to the corresponding ones for the proton beam. Specifically, we see the following.

(1) At low P_T the values of α_i approach a value of approximately $\frac{2}{3}$, as expected from the area of a black disk.

TABLE XIV. The ratios of the invariant cross sections for $\pi^\pm$, $K^\pm$, p, and $\bar{p}$ production in 200 GeV $\pi^- p$ collisions to that in 200 GeV pp collisions ("beam ratios") versus P_T.

P_T (GeV/c)	π^+	π^-	K^+	K^-	p	$\bar{p}$
0.96	0.58 ± 0.06	0.79 ± 0.08	0.72 ± 0.09	0.97 ± 0.13	0.54 ± 0.06	1.03 ± 0.13
1.44	0.55 ± 0.06	0.80 ± 0.08	0.55 ± 0.07	0.86 ± 0.10	0.37 ± 0.04	1.04 ± 0.12
1.93	0.64 ± 0.07	0.93 ± 0.10	0.61 ± 0.07	1.00 ± 0.13	0.41 ± 0.05	1.45 ± 0.19
2.41	0.69 ± 0.04	1.00 ± 0.06	0.72 ± 0.05	1.16 ± 0.08	0.42 ± 0.03	1.41 ± 0.14
2.89	0.77 ± 0.06	1.29 ± 0.10	0.77 ± 0.07	1.43 ± 0.16	0.41 ± 0.04	1.97 ± 0.25
3.85	1.12 ± 0.13	1.88 ± 0.21	1.05 ± 0.17	2.71 ± 0.54	0.50 ± 0.09	3.50 ± 1.30
4.82	1.11 ± 0.32	3.80 ± 1.10	1.07 ± 0.45	----------	0.54 ± 0.34	----------

TABLE XV. The invariant cross sections versus P_T for the production of hadrons in 200 GeV π^-Be collisions. The laboratory angle was 96.3 mrad, which corresponds to a c.m. production angle of ~90° for highly relativistic secondary particles.

P_T (GeV/c)	π^+	π^-	K^+	K^-	p	$\bar{p}$
0.96	$2.68 \pm 0.22 \times 10^{-27}$	$3.40 \pm 0.28 \times 10^{-27}$	$7.55 \pm 0.69 \times 10^{-28}$	$6.10 \pm 0.58 \times 10^{-28}$	$9.46 \pm 0.79 \times 10^{-28}$	$3.40 \pm 0.31 \times 10^{-28}$
1.44	$2.42 \pm 0.20 \times 10^{-28}$	$3.18 \pm 0.26 \times 10^{-28}$	$8.25 \pm 0.70 \times 10^{-29}$	$6.37 \pm 0.54 \times 10^{-29}$	$1.14 \pm 0.09 \times 10^{-28}$	$4.53 \pm 0.38 \times 10^{-29}$
1.93	$2.82 \pm 0.23 \times 10^{-29}$	$3.53 \pm 0.28 \times 10^{-29}$	$1.04 \pm 0.09 \times 10^{-29}$	$8.89 \pm 0.74 \times 10^{-30}$	$1.44 \pm 0.12 \times 10^{-29}$	$5.12 \pm 0.43 \times 10^{-30}$
2.41	$3.21 \pm 0.15 \times 10^{-30}$	$4.60 \pm 0.21 \times 10^{-30}$	$1.40 \pm 0.07 \times 10^{-30}$	$1.13 \pm 0.06 \times 10^{-30}$	$1.47 \pm 0.07 \times 10^{-30}$	$5.02 \pm 0.29 \times 10^{-31}$
2.89	$4.32 \pm 0.26 \times 10^{-31}$	$6.73 \pm 0.38 \times 10^{-31}$	$2.22 \pm 0.17 \times 10^{-31}$	$1.69 \pm 0.15 \times 10^{-31}$	$1.89 \pm 0.14 \times 10^{-31}$	$4.65 \pm 0.61 \times 10^{-32}$
3.85	$1.76 \pm 0.27 \times 10^{-32}$	$2.21 \pm 0.30 \times 10^{-32}$	$6.92 \pm 1.77 \times 10^{-33}$	$7.47 \pm 1.85 \times 10^{-33}$	$7.63 \pm 1.76 \times 10^{-33}$	$2.72 \pm 2.74 \times 10^{-34}$
4.82	$1.01 \pm 0.30 \times 10^{-33}$	$1.21 \pm 0.33 \times 10^{-33}$	$3.82 \pm 1.94 \times 10^{-34}$	$3.18 \pm 1.86 \times 10^{-34}$	$9.15 \pm 9.13 \times 10^{-35}$	------------------
5.78	$1.23 \pm 1.24 \times 10^{-35}$	$7.55 \pm 3.85 \times 10^{-35}$	------------------	------------------	------------------	------------------

TABLE XVI. The invariant cross sections versus P_T for the production of hadrons in 200 GeV π^-Cu collisions. The laboratory angle was 96.3 mrad, which corresponds to a c.m. production angle of ~90° for highly relativistic secondary particles. Data were taken only at values of 2.4 and 2.9 GeV/c because of limited running time.

P_T (GeV/c)	π^+	π^-	K^+	K^-	p	$\bar{p}$
0.96	------------------	------------------	------------------	------------------	------------------	------------------
1.44	------------------	------------------	------------------	------------------	------------------	------------------
1.93	------------------	------------------	------------------	------------------	------------------	------------------
2.40	$2.31 \pm 0.11 \times 10^{-29}$	$3.13 \pm 0.15 \times 10^{-29}$	$1.12 \pm 0.06 \times 10^{-29}$	$8.16 \pm 0.44 \times 10^{-30}$	$1.36 \pm 0.07 \times 10^{-29}$	$4.10 \pm 0.23 \times 10^{-30}$
2.89	$3.94 \pm 0.20 \times 10^{-30}$	$5.56 \pm 0.27 \times 10^{-30}$	$1.98 \pm 0.12 \times 10^{-30}$	$1.40 \pm 0.09 \times 10^{-30}$	$2.14 \pm 0.12 \times 10^{-30}$	$6.30 \pm 0.47 \times 10^{-31}$
3.85	------------------	------------------	------------------	------------------	------------------	------------------
4.82	------------------	------------------	------------------	------------------	------------------	------------------
5.78	------------------	------------------	------------------	------------------	------------------	------------------

TABLE XVII. The invariant cross sections versus P_T for the production of hadrons in 200 GeV π^-W collisions. The laboratory angle was 96.3 mrad, which corresponds to a c.m. production angle of ~90° for highly relativistic secondary particles.

P_T (GeV/c)	π^+	π^-	K^+	K^-	p	$\bar{p}$
0.96	$3.76 \pm 0.31 \times10^{-26}$	$4.35 \pm 0.35 \times10^{-26}$	$1.37 \pm 0.12 \times10^{-26}$	$1.05 \pm 0.09 \times10^{-26}$	$1.71 \pm 0.14 \times10^{-26}$	$4.48 \pm 0.39 \times10^{-27}$
1.44	$4.12 \pm 0.34 \times10^{-27}$	$4.92 \pm 0.40 \times10^{-27}$	$1.58 \pm 0.14 \times10^{-27}$	$1.24 \pm 0.11 \times10^{-27}$	$2.33 \pm 0.19 \times10^{-27}$	$7.48 \pm 0.63 \times10^{-28}$
1.93	$5.33 \pm 0.43 \times10^{-28}$	$6.87 \pm 0.56 \times10^{-28}$	$2.31 \pm 0.20 \times10^{-28}$	$1.82 \pm 0.16 \times10^{-28}$	$3.59 \pm 0.29 \times10^{-28}$	$1.04 \pm 0.09 \times10^{-28}$
2.41	$7.67 \pm 0.35 \times10^{-29}$	$1.04 \pm 0.47 \times10^{-28}$	$3.73 \pm 0.18 \times10^{-29}$	$2.77 \pm 0.13 \times10^{-29}$	$4.83 \pm 0.22 \times10^{-29}$	$1.38 \pm 0.07 \times10^{-29}$
2.89	$1.26 \pm 0.06 \times10^{-29}$	$1.71 \pm 0.08 \times10^{-29}$	$6.34 \pm 0.38 \times10^{-30}$	$5.17 \pm 0.32 \times10^{-30}$	$7.23 \pm 0.40 \times10^{-30}$	$1.87 \pm 0.14 \times10^{-30}$
3.85	$3.95 \pm 0.23 \times10^{-31}$	$6.31 \pm 0.36 \times10^{-31}$	$2.28 \pm 0.16 \times10^{-31}$	$1.54 \pm 0.14 \times10^{-31}$	$2.12 \pm 0.15 \times10^{-31}$	$5.24 \pm 0.67 \times10^{-32}$
4.82	$1.70 \pm 0.15 \times10^{-32}$	$3.06 \pm 0.24 \times10^{-32}$	$9.20 \pm 1.06 \times10^{-33}$	$7.60 \pm 1.10 \times10^{-33}$	$6.06 \pm 0.77 \times10^{-33}$	$1.60 \pm 0.48 \times10^{-33}$
5.78	$4.66 \pm 1.33 \times10^{-34}$	$1.34 \pm 0.26 \times10^{-33}$	$5.74 \pm 1.64 \times10^{-34}$	$3.81 \pm 1.47 \times10^{-34}$	$1.84 \pm 0.83 \times10^{-34}$	-----------------

TABLE XVIII. The invariant cross sections versus P_T for the production of hadrons in 300 GeV π^-W collisions. The laboratory angle was 80 mrad, which corresponds to a production angle of ~90° for highly relativistic secondary particles.

P_T (GeV/c)	π^+	π^-	K^+	K^-	p	$\bar{p}$
0.80	$1.01 \pm 0.08 \times10^{-25}$	$1.13 \pm 0.09 \times10^{-25}$	$2.99 \pm 0.29 \times10^{-26}$	$2.67 \pm 0.26 \times10^{-26}$	$3.39 \pm 0.29 \times10^{-26}$	$1.04 \pm 0.10 \times10^{-26}$
1.20	$1.45 \pm 0.12 \times10^{-26}$	$1.66 \pm 0.14 \times10^{-26}$	$5.12 \pm 0.45 \times10^{-27}$	$3.98 \pm 0.35 \times10^{27}$	$6.74 \pm 0.56 \times10^{-27}$	$2.53 \pm 0.22 \times10^{-27}$
1.60	$2.52 \pm 0.21 \times10^{-27}$	$3.06 \pm 0.25 \times10^{-27}$	$1.05 \pm 0.09 \times10^{-27}$	$8.71 \pm 0.75 \times10^{-28}$	$1.37 \pm 0.11 \times10^{-27}$	$5.29 \pm 0.46 \times10^{-28}$
2.00	$5.10 \pm 0.25 \times10^{-28}$	$6.62 \pm 0.32 \times10^{-28}$	$2.22 \pm 0.12 \times10^{-28}$	$1.85 \pm 0.11 \times10^{-28}$	$2.98 \pm 0.15 \times10^{-28}$	$1.14 \pm 0.07 \times10^{-28}$
2.40	$1.24 \pm 0.06 \times10^{-28}$	$1.63 \pm 0.08 \times10^{-28}$	$5.63 \pm 0.34 \times10^{-29}$	$4.47 \pm 0.28 \times10^{-29}$	$7.01 \pm 0.38 \times10^{-29}$	$2.47 \pm 0.17 \times10^{-29}$
3.20	$7.17 \pm 0.43 \times10^{-30}$	$1.01 \pm 0.06 \times10^{-29}$	$3.71 \pm 0.28 \times10^{-30}$	$3.45 \pm 0.27 \times10^{-30}$	$3.72 \pm 0.27 \times10^{-30}$	$1.20 \pm 0.13 \times10^{-30}$
4.00	$6.38 \pm 0.43 \times10^{-31}$	$8.75 \pm 0.53 \times10^{-31}$	$3.09 \pm 0.27 \times10^{-31}$	$2.48 \pm 0.23 \times10^{-31}$	$2.61 \pm 0.23 \times10^{-31}$	$6.90 \pm 1.02 \times10^{-32}$
4.80	$5.63 \pm 0.61 \times10^{-32}$	$7.91 \pm 0.82 \times10^{-32}$	$2.22 \pm 0.36 \times10^{-32}$	$2.82 \pm 0.48 \times10^{-32}$	$1.72 \pm 0.31 \times10^{-32}$	$3.36 \pm 1.53 \times10^{-33}$
5.60	-----------------	$9.71 \pm 1.76 \times10^{-33}$	-----------------	$1.97 \pm 0.76 \times10^{-33}$	-----------------	-----------------
6.40	-----------------	$1.60 \pm 0.40 \times10^{-33}$	-----------------	-----------------	-----------------	-----------------

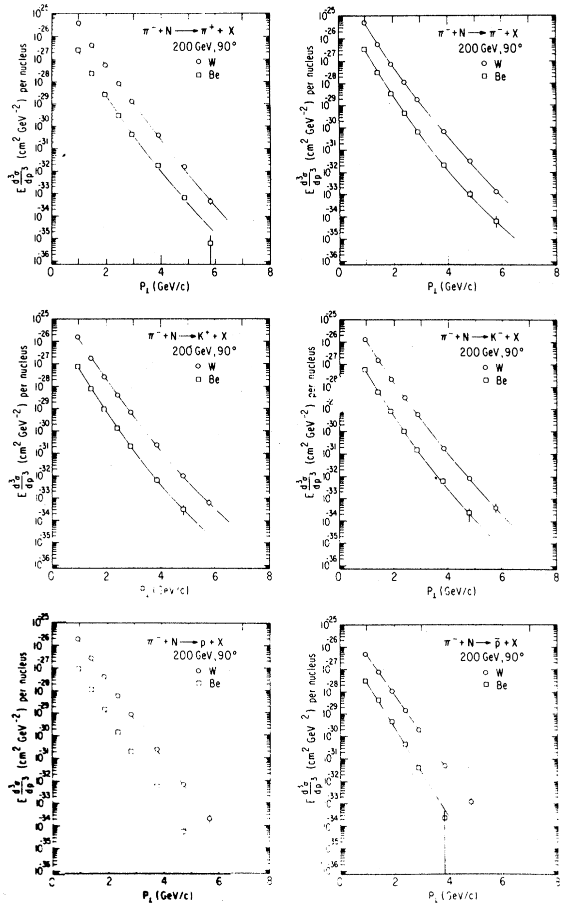

FIG. 31. The cross sections per nucleus for hadron production versus P_T in π^-Be and π^-W collisions at 200 GeV. All data are at a laboratory angle of 97 mrad, which corresponds to ~90° in the π^- nucleon c.m. for highly relativistic secondaries. The relative spacing of the lines, which are drawn by eye, gives the effective A dependence. Errors on the data points are too small to be seen.

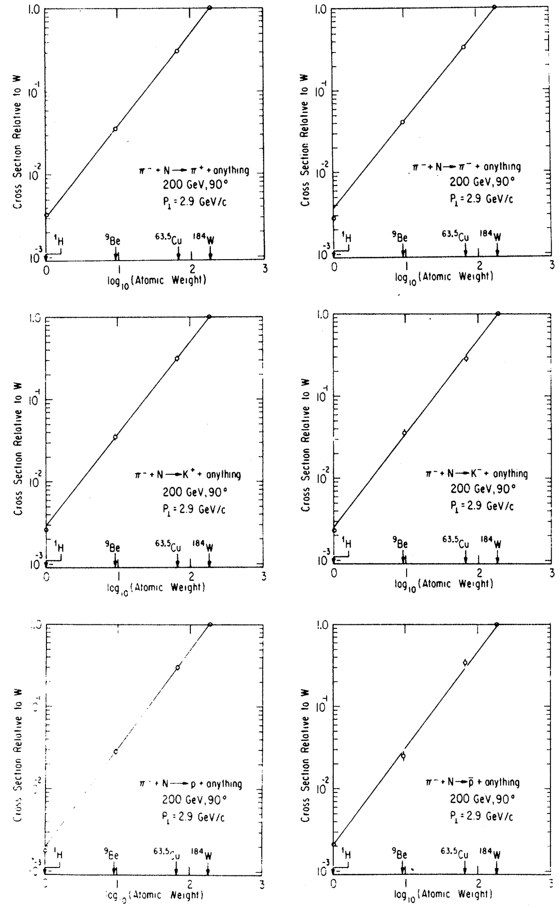

FIG. 32. The cross sections per nucleus relative to the cross section per W nucleus, versus the atomic weight A of the target, at a value of P_T=2.9 GeV/c. The data points for hydrogen were not included in the fit, which is represented by the straight line.

(2) For P_T values ≥ 3 GeV/c the values of α_i exceed the value 1, an indication that the nucleus acts in some collective way.

(3) The $\alpha_{\pi^\pm}$ and $\alpha_{K^\pm}$ flatten at P_T=4 GeV/c, at values ~1.1 or so.

(4) $\alpha_{\pi^\pm}$ and $\alpha_{K^\pm}$ show an indication of decreasing at $P_T > 4$ GeV/c, but it is statistically not proven.

(5) α_p and $\alpha_{\bar{p}}$ seem to rise to much higher values than the rest of the exponents, but again the statistics are not overwhelming (we note that an α value of 1.5 corresponds to a nucleus which, if the nucleons acted independently, would have 2500 nucleons).

The exponents measured with the proton beam are slightly higher than those measured with the π^- beam at the low-P_T (1—3 GeV/c) region. This is consistent with the small $\sqrt{s}$ dependence observed[8] at low P_T with proton beams.

VI. CONCLUSIONS

We have measured the cross section in 200 GeV and 300 GeV $\pi^- p$ and π^--nucleus collisions for the production of identified charged hadrons over the P_T range $0.8 < P_T < 6.4$ GeV/c. Data at three different laboratory production angles allow a measurement of the angular dependence of the cross sections. Data also taken with the same apparatus on pp and p-nucleus collisions permit a comparison of the production of charged hadrons in $\pi^- p$ (π^--nucleus) and pp (p-nucleus) collisions.

TABLE XIX. The values of α_i in the fitted form A^{α_i} for each particle type versus P_T, from 200 GeV π^--nucleus collisions.

P_T (GeV/c)	$\alpha(\pi^+)$	$\alpha(\pi^-)$	$\alpha(K^+)$	$\alpha(K^-)$	$\alpha(p)$	$\alpha(\bar{p})$
0.96	0.88 ± 0.01	0.85 ± 0.01	0.96 ± 0.02	0.94 ± 0.02	0.96 ± 0.01	0.86 ± 0.02
1.44	0.94 ± 0.01	0.91 ± 0.01	0.98 ± 0.02	0.98 ± 0.02	1.00 ± 0.01	0.93 ± 0.02
1.93	0.97 ± 0.01	0.99 ± 0.01	1.03 ± 0.02	1.00 ± 0.02	1.07 ± 0.01	1.00 ± 0.02
2.41	1.05 ± 0.01	1.03 ± 0.01	1.09 ± 0.01	1.06 ± 0.01	1.16 ± 0.01	1.10 ± 0.02
2.89	1.12 ± 0.02	1.07 ± 0.02	1.11 ± 0.03	1.13 ± 0.03	1.21 ± 0.02	1.22 ± 0.05
3.85	1.03 ± 0.05	1.11 ± 0.04	1.16 ± 0.09	1.00 ± 0.09	1.10 ± 0.08	1.74 ± 0.34
4.82	.94 ± 0.10	1.10 ± 0.09	1.06 ± 0.17	1.05 ± 0.20	1.39 ± 0.33	--------
5.78	1.21 ± 0.35	0.99 ± 0.18	--------	--------	--------	--------

The conclusions we draw, briefly stated, are as follows.

A. Scaling of π^-p cross sections

The π^-p invariant cross sections scale in the sense that they are well fitted by the form $E\,d^3\sigma/dp^3=A(1-x_T)^b/p_T{}^n$, where $x_T=2p_T/\sqrt{s}$. The values of b and n for the six particle types are presented in Table VI, and are compared in this table to the values derived in 400 GeV pp collisions.

For $\pi^\pm$ and $K^\pm$ high-P_T production the fitted values for n (the power of $1/P_T$) are consistent with a value of 8, which is the value observed for these reactions in pp collisions at these energies.[8] This value is less than the value of 10 observed previously for π^0 production in 100 and 200 GeV π^- col-

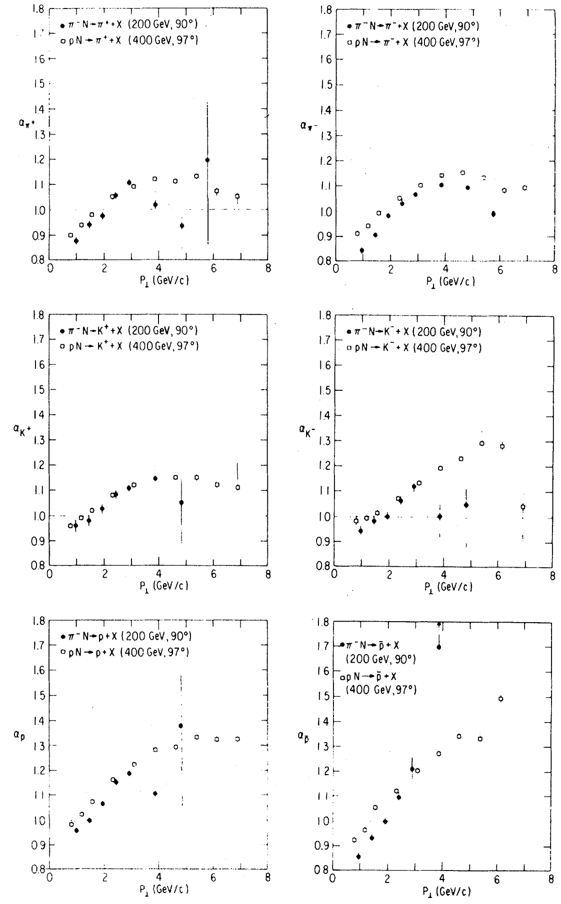

FIG. 33. The values of α_i (solid circles) derived from fits to the form A^{α_i}, versus P_T for each of the six particle types $i=\pi^\pm$, $K^\pm$, p, and $\bar{p}$ produced in 200 GeV π^-p collisions. Also shown (open squares) are the data from Ref. 8 for 400 GeV proton-nucleus collisions at an 80 mrad laboratory angle.

lisions.[21] The values of n for p and $\bar{p}$ production are both about 10, and are more alike than in the pp case.

The values of b tend to be lower (especially for K^- and $\bar{p}$'s) than in the pp case, presumably due to fewer quarks sharing the momentum in the initial state.

B. Comparison of $\pi^- p$ cross sections to pp cross sections

(1) At large x_T, $\pi^- p$ collisions produce significantly more π^-, K^-, and $\bar{p}$ than pp collisions (see Figs. 28, 29, and 30). The average relative production of pions, $(\pi^+ + \pi^-)/2$, agrees well with π^0 production as measured by Donaldson *et al.*[5] (see Fig. 27).

(2) Despite two units of positive charge less in the initial state, $\pi^- p$ collisions are equally effective at producing π^+ and K^+ at large P_T as pp collisions.

(3) The production of protons in π^- collisions, however, is half that in pp collisions. (We note that there are also half as many protons in the initial state.)

(4) The predictions for meson production are fit well by a QCD model calculation of Field.[23]

C. The antiparticle/particle ratios in $\pi^- p$ collisions

(1) The charge ratios of the produced particles, i.e., π^-/π^+, K^-/K^+, and $\bar{p}/p$ are quite different in $\pi^- p$ collisions from those in pp collisions. The π^-/π^+ ratio, for instance, is consistent with being flat even at substantial values of x_T, rather than falling as in pp collisions. It is well fit by QCD model calculations, although it is thoroughly inconsistent with previously published CIM calculations. (See Fig. 15).

(2) The K^-/K^+ and $\bar{p}/p$ ratios fall much less steeply in P_T in $\pi^- p$ collisions than in pp collisions. (See Figs. 16 and 17.)

D. Particle ratios K^+/π^+, K^-/π^-, p/π^+, $\bar{p}/\pi^-$ in $\pi^- p$ collisions

(1) The ratio of K^+/π^+ in $\pi^- p$ collisions is indistinguishable from that in pp collisions, and levels off at ~ 0.5. This ratio is consistent with the u quark having only half as many $\bar{s}$ as $\bar{d}$ quarks to pick up from the sea.

(2) The ratio of p/π^+ is appreciably less than that observed in pp collisions at the same energy.

(3) Both the K^-/π^- and $\bar{p}/\pi^-$ ratios are enhanced in $\pi^- p$ collisions over the ratios in pp scattering, especially at large P_T.

E. The angular dependence of cross sections in $\pi^- p$ collisions

Cross sections versus P_T were measured at laboratory angles of 96, 80, and 63 mrad, corresponding to c.m. angles of approximately 90°, 79°, and 67°. The angular dependence is fairly weak. Calculations[23] have found it necessary to invoke a stiffer gluon fragmentation function to fit the data. We consider this angular dependence in $\pi^- p$ collisions a fruitful area to explore, as one can attempt to untangle to some extent the relative π and proton contributions.

F. The atomic-weight dependence

The cross sections have been measured on Be, Cu (at two momenta), and W targets. The data have been parametrized by the form A^{α_i}, where i refers to the particle type $\pi^\pm$, $K^\pm$, p, or $\bar{p}$. The exponents α_i grow to be greater than 1 in a manner very similar to that seen in pp scattering.

ACKNOWLEDGMENTS

We would like to thank the many people who have helped us on this experiment. We wish to thank Ken Stanfield, Jon Hawkins, Al Guthke, Ron Currier and the staff of the Proton Laboratory of Fermilab for their willing help in the construction of the apparatus and the operation of the high-intensity beam. We also thank Carl Bopp, Ann David, Marius Isaila, John Quinn, Howard Edwards, and the members of the Elementary Particles Laboratory at Princeton, and Dick Armstrong, Harold Sanders and the staffs of the electronic and engineering support groups of the Enrico Fermi Institute, for much help in the design, building and operation of the experiment. We owe a great deal to Jim Cronin for his initial participation. Chad Edwards, Mike Halling, and Chuck Whitmer each made contributions to the running of the experiment. Steve Ellis, Rick Field, Neil Fleishon, and James Stirling have been of great help in understanding the data. We extend thanks also to Dale Boyce of the University of Chicago for his beam-flux measurements with the ^{24}Na and ^{57}Co cross sections.

This experiment was supported by the Department of Energy and the National Science Foundation. One of us (M.J.S.) would also like to thank the Alfred P. Sloan Foundation.

[*] Present address: Department of Physics, University of Rochester, River Campus Station, Rochester, N. Y. 14627.

[†] Present address: Serin Physics Laboratory, Rutgers State University, Frelinghuysen Road, Piscataway, N. J. 08854.

[‡] Present address: Department of Physics and Astronomy, Vanderbilt University, Nashville, Tennessee 37235.

[§] Present address: Bell Laboratories, Murray Hill, N. J. 07974.

[1] H. J. Frisch *et al.*, Phys. Rev. Lett. 44, 511 (1980).

[2] N. D. Giokaris *et al.*, Phys. Rev. Lett. 47, 1690 (1981).

[3] J. M. Green, Ph.D. thesis, University of Chicago, 1981 (unpublished).

[4] N. D. Giokaris, Ph.D. thesis, University of Chicago, 1981 (unpublished).

[5] G. Donaldson *et al.*, Phys. Rev. Lett. 36, 1110 (1976); Phys. Lett. 73B, 375 (1978); Phys. Rev. Lett. 40, 917 (1978); Report No. BNL-23844 (unpublished) (a compilation of the numerical values).

[6] C. Bromberg *et al.*, Phys. Rev. Lett. 43, 561 (1979); Nucl. Phys. B171, 38 (1980).

[7] M. D. Corcoran *et al.*, Phys. Rev. Lett. 41, 9 (1978); Phys. Rev. D 19, 1361 (1979); *ibid.* 21, 641 (1980); Phys. Rev. Lett. 44, 514 (1980).

[8] D. Antreasyan *et al.*, Phys. Rev. D 19, 764 (1979).

[9] The beam as conceived is described in B. Cox *et al.*, report, 1977 (unpublished).

[10] J. W. Cronin *et al.*, E258 proposal at Fermilab, 1973 (unpublished).

[11] Ch. Iselin, HALO, a computer program to calculate muon halo, Report No. CERN 74-17, 1974 (unpublished).

[12] W. F. Baker *et al.*, Report No. NAL-Pub-74/13-Exp. 7100.104 (unpublished); H. W. Atherton *et al.*, Report No. CERN 80-70, SPS Division, 1980 (unpublished).

[13] For a detailed description of these magnets see, for example, T. Toohig, Fermilab Report No. TM-632/2200.00/1975, revised version (unpublished).

[14] H. J. Frisch *et al.*, IEEE Trans Nucl. Sci. NS-27, 150 (1980).

[15] J. Allaby *et al.*, Yad. Fiz. 12, 538 (1971) [Sov. J. Nucl. Phys. 12, 295 (1971)].

[16] F. Sauli, Report No. CERN 77-09, 1977 (unpublished).

[17] D. Boyce, University of Chicago (private communication); A. Chapman-Hatchett *et al.*, CERN Report No. SPS/ABT/Int 79-1, 1979 (unpublished).

[18] S. J. Brodsky and G. R. Farrar, Phys. Rev. Lett. 31, 1153 (1973); V. A. Matveev, R. M. Muradyan, and A. N. Tavkhelidze, Lett. Nuovo Cimento 7, 719 (1973).

[19] S. M. Berman, J. D. Bjorken, and J. B. Kogut, Phys. Rev. D 4, 3388 (1971).

[20] A. G. Clark *et al.*, Phys. Lett. 74B, 267 (1978); A. L. S. Angelis *et al.*, *ibid.* 79B, 505 (1978).

[21] See Ref. 5. In fact, the fit of Ref. 5 was performed to a parametrization slightly different from the simple one given above, viz.,

$$E\,d^3\sigma/dp^3 \simeq \frac{1}{(P_T+m)^n} f(x_T)\,.$$

The conclusions, in particular the agreement between the values of n in π^-p and pp collisions, are unchanged.

[22] See, for example, N. Fleishon and J. Stirling, Nucl. Phys. B188, 205 (1981).

[23] R. D. Field (private communication). For a description of the model, see R. P. Feynman, R. D. Field, and G. C. Fox, Nucl. Phys. B128, 1 (1977).

[24] J. Gunion and D. Jones, Phys. Rev. D 19, 867 (1979).

[25] The measurements of the Harvard-Pennsylvania-Wisconsin-Fermilab group give an $\bar{s}/\bar{d}$ ratio of ~0.5, those of the CERN-Dortmund-Heidelberg-Saclay Collaboration ~0.24. See, for example, the nice review by A. Para, in the Proceedings of the EPS International Conference on High Energy Physics, Lisbon, Portugal, 1981, edited by J. Dias de Deus and J. Soffer (unpublished).

[26] Because these particle ratios in π^-p collisions are not changing rapidly with P_T (see Fig. 23), we have used data from $P_T = 3.85$ GeV/c at $\theta_{\text{c.m.}} = 90°$, $P_T = 4$ GeV/c at $\theta_{\text{c.m.}} = 79°$, and $P_T = 3.82$ GeV/c at $\theta_{\text{c.m.}} = 67°$.

[27] See, for example, Particle Data Group, Rev. Mod. Phys. 52, S1 (1980).

[28] G. R. Farrar, Phys. Lett. 56B, 185 (1975).

[29] J. H. Kühn, Phys. Rev. D 13, 2948 (1976).

[30] A. Krzywicki, Phys. Rev. D 14, 152 (1976).

[31] A. Krzywicki, J. Engels, B. Petersson, and U. Sukhatme, Phys. Lett. 85B, 407 (1979).